



## A finite volume numerical approach for coastal ocean circulation studies: Comparisons with finite difference models

Changsheng Chen,<sup>1,2,3</sup> Haosheng Huang,<sup>1</sup> Robert C. Beardsley,<sup>4</sup> Hedong Liu,<sup>1</sup> Qichun Xu,<sup>1</sup> and Geoffrey Cowles<sup>1</sup>

Received 10 January 2006; revised 4 June 2006; accepted 9 August 2006; published 28 March 2007.

[1] An unstructured grid, finite volume, three-dimensional (3-D) primitive equation coastal ocean model (FVCOM) has been developed for the study of coastal ocean and estuarine circulation by Chen et al. (2003a). The finite volume method used in this model combines the advantage of finite element methods for geometric flexibility and finite difference methods for simple discrete computation. Currents, temperature, and salinity are computed using an integral form of the equations, which provides a better representation of the conservative laws for mass, momentum, and heat. Detailed comparisons are presented here of FVCOM simulations with analytical solutions and numerical simulations made with two popular finite difference models (the Princeton Ocean Model and Estuarine and Coastal Ocean Model (ECOM-si)) for the following idealized cases: wind-induced long-surface gravity waves in a circular lake, tidal resonance in rectangular and sector channels, freshwater discharge onto the continental shelf with curved and straight coastlines, and the thermal bottom boundary layer over the slope with steep bottom topography. With a better fit to the curvature of the coastline using unstructured nonoverlapping triangle grid cells, FVCOM provides improved numerical accuracy and correctly captures the physics of tide-, wind-, and buoyancy-induced waves and flows in the coastal ocean. This model is suitable for applications to estuaries, continental shelves, and regional basins that feature complex coastlines and bathymetry.

**Citation:** Chen, C., H. Huang, R. C. Beardsley, H. Liu, Q. Xu, and G. Cowles (2007), A finite volume numerical approach for coastal ocean circulation studies: Comparisons with finite difference models, *J. Geophys. Res.*, 112, C03018, doi:10.1029/2006JC003485.

### 1. Introduction

[2] The most difficult technical issues in coastal ocean modeling are to (1) resolve the irregular coastal geometry and (2) ensure conservation of momentum, mass, and heat. In the last decade, finite difference and finite element methods have been widely used in ocean modeling. The most popular finite difference and finite element coastal ocean models are the Princeton Ocean Model (POM) [Blumberg and Mellor, 1987], the semi-implicit Estuarine and Coastal Ocean Model (ECOM-si) [Blumberg, 1994], the Regional Ocean Model (ROM) [Haidvogel et al., 2000], and the Dartmouth College Model (QUODDY) [Lynch and Naimie, 1993; Naimie, 1996]. The finite difference method has its advantage in simple code structure and computational efficiency. This method, however, is limited because

of difficulty in accurately fitting irregular coastal geometry. Introducing an orthogonal or nonorthogonal curvilinear coordinate transformation into a finite difference model can provide a moderate fitting of coastal boundaries, but these transformations are incapable of resolving the coastal boundaries characterized by numerous barrier islands and tidal creek complexes. The greatest advantage of the finite element method is its geometric flexibility. Unstructured triangular meshes used in this method can provide an accurate fitting of irregular coastal boundaries. The traditional finite element method, however, usually involves an extensive large size matrix calculation at every time step, which is achieved at the expense of computational efficiency. Because the governing equations are numerically solved through a least squares variational method, the finite element method, however, does not provide an explicit way to check the mass conservation in individual cells during the computation. The p-type finite element method [Maday and Patera, 1988] or discontinuous Galerkin method [Reed and Hill, 1973; Cockburn et al., 1990] have been introduced into updated finite element techniques. Application of these methods to current finite element coastal ocean models could significantly improve computational accuracy and efficiency as well as mass conservation [Hughes et al., 2000].

<sup>1</sup>School of Marine Sciences and Technology (SMASST), University of Massachusetts-Dartmouth, New Bedford, Massachusetts, USA.

<sup>2</sup>Now at Department of Physical Oceanography, Woods Hole Oceanographic Institution, Woods Hole, Massachusetts, USA.

<sup>3</sup>Also at The Sate Key Laboratory for Estuarine and Coastal Research, East China Normal University, Shanghai, China.

<sup>4</sup>Department of Physical Oceanography, Woods Hole Oceanographic Institution, Woods Hole, Massachusetts, USA.

[3] Recently, we have developed an unstructured grid, finite volume, three-dimensional primitive equation, coastal ocean model (FVCOM) [Chen *et al.*, 2003a]. Unlike differential forms used in a finite difference model, FVCOM discretizes the integral form of the governing equations. Since these integral equations can be solved numerically by flux calculation used in the finite difference method over arbitrarily sized triangular meshes, the finite volume approach is better at guaranteeing mass conservation in both individual control elements and the entire computational domain. In view of this technical approach, FVCOM combines the best attributes of finite difference methods for simple discrete computational efficiency and finite element methods for geometric flexibility. This model has been successfully applied to studies of flow in a number of estuaries and coastal oceans that are characterized by complex irregular geometry, intertidal flooding/drying processes, steeply sloping bottom topography, etc. (see <http://fvcom.smast.umassd.edu>).

[4] One common method used to evaluate an ocean model is to compare the model results with observations. While such comparison can be extremely useful, problems with sparse data and possibility of obtaining a good model/data fit for improper physical reasons limit this approach to model validation. In order to provide an objective evaluation of FVCOM, numerical experiments were conducted to compare FVCOM with analytical solutions for the following idealized cases: wind-induced long-surface gravity waves in a circular lake; tidal resonance in an semienclosed channel; freshwater discharge over the continental shelf with curved and straight coastlines; and the thermal boundary layer over the slope with steep bottom topography. Comparisons were also made with structured grid finite difference models versus analytical solutions to examine the impact of geometric fitting on the accuracy of the numerical solution. The Princeton Ocean Model (POM) and its semi-implicit version (ECOM-si) were selected as representative of structured grid finite difference models in model validation experiments. POM and ECOM-si [Blumberg and Mellor, 1987] are two reliable finite difference ocean models that have dominated coastal ocean modeling in the last 20 years. The development of FVCOM was motivated by our failure to apply POM and ECOM-si to resolve the complex irregular geometries of tidal creeks in an estuarine application. Since FVCOM and POM/ECOM-si describe the same dynamics, comparisons between these models provide us with an objective view on the impact of coastal geometry on the coastal and estuarine physics.

[5] This paper summarizes the validation experiment results with the focus on the evaluation of the need for unstructured grid meshes for coastal ocean modeling application. Although the comparison was made between FVCOM and POM/ECOM-si, the results are generally applicable to any unstructured and structured grid ocean models.

[6] The rest of this paper is structured as follows. FVCOM, POM, and ECOM-si are briefly described in section 2. The comparison results for the four idealized cases are presented in section 3, followed by several examples of application of FVCOM and POM/ECOM-si to tidal processes in the Gulf of Maine/Georges Bank region

in section 4. Discussion and conclusions are presented in section 5.

## 2. Models

[7] Numerical models used in this study consist of seven primitive ocean governing equations (three for momentum, one for incompressible continuity, two for temperature and salinity, and one for density) [Blumberg and Mellor, 1987; Chen *et al.*, 2003a]. They are prognostic models with a free surface and are mathematically closed using the modified Mellor and Yamada level-2.5 (MY-2.5) turbulent closure scheme for vertical mixing [Mellor and Yamada, 1982; Galperin *et al.*, 1988]. The models use the  $\sigma$ -transformation in the vertical to convert irregular bottom topography into a rectangular computational domain for simple numerical approach. The governing equations for motion, temperature, salinity and density are given as

$$\begin{aligned} & \frac{\partial uD}{\partial t} + \frac{\partial u^2D}{\partial x} + \frac{\partial uvD}{\partial y} + \frac{\partial u\omega}{\partial \sigma} - f v D \\ &= -gD \frac{\partial \zeta}{\partial x} - \frac{gD}{\rho_o} \left[ \frac{\partial}{\partial x} \left( D \int_{\sigma}^0 \rho' d\sigma' \right) + \sigma \rho' \frac{\partial D}{\partial x} \right] \\ &+ \frac{1}{D} \frac{\partial}{\partial \sigma} \left( K_m \frac{\partial u}{\partial \sigma} \right) + DF_x \end{aligned} \quad (1)$$

$$\begin{aligned} & \frac{\partial vD}{\partial t} + \frac{\partial uvD}{\partial x} + \frac{\partial v^2D}{\partial y} + \frac{\partial v\omega}{\partial \sigma} + f u D \\ &= -gD \frac{\partial \zeta}{\partial y} - \frac{gD}{\rho_o} \left[ \frac{\partial}{\partial y} \left( D \int_{\sigma}^0 \rho' d\sigma' \right) + \sigma \rho' \frac{\partial D}{\partial y} \right] \\ &+ \frac{1}{D} \frac{\partial}{\partial \sigma} \left( K_m \frac{\partial v}{\partial \sigma} \right) + DF_y \end{aligned} \quad (2)$$

$$\frac{\partial TD}{\partial t} + \frac{\partial TuD}{\partial x} + \frac{\partial TvD}{\partial y} + \frac{\partial T\omega}{\partial \sigma} = \frac{1}{D} \frac{\partial}{\partial \sigma} \left( K_h \frac{\partial T}{\partial \sigma} \right) + D\hat{H} + DF_T \quad (3)$$

$$\frac{\partial SD}{\partial t} + \frac{\partial SuD}{\partial x} + \frac{\partial SvD}{\partial y} + \frac{\partial S\omega}{\partial \sigma} = \frac{1}{D} \frac{\partial}{\partial \sigma} \left( K_h \frac{\partial S}{\partial \sigma} \right) + DF_S \quad (4)$$

$$\rho = \rho(T, S) \quad (5)$$

where  $x$ ,  $y$ , and  $\sigma$  are the east, north, and vertical axes of the  $\sigma$ -coordinate;  $u$ ,  $v$ , and  $\omega$  are the  $x$ ,  $y$ ,  $\sigma$  velocity components;  $D$  is the total depth equal to a sum of mean depth  $H$  and surface elevation  $\zeta$ ;  $T$  is the temperature;  $S$  is the salinity;  $\rho$  is the total density equal to a sum of perturbation density  $\rho'$  and reference density  $\rho_o$ ;  $f$  is the Coriolis parameter;  $g$  is the gravitational acceleration;  $K_m$  is the vertical eddy viscosity coefficient;  $K_h$  is the thermal vertical eddy diffusion coefficient;  $F_u$ ,  $F_v$ ,  $F_T$ , and  $F_S$  represent the horizontal momentum, thermal, and salt diffusion terms; and  $\hat{H}$  is the absorption of downward shortwave irradiance.  $K_m$  and  $K_h$  are parameterized using

the MY-2.5 turbulence submodel, and horizontal diffusion coefficients are determined using a Smagorinsky eddy parameterization method [Smagorinsky, 1963].

[8] The surface and bottom boundary conditions for  $u$ ,  $v$ , and  $w$  are specified as

$$\left(\frac{\partial u}{\partial \sigma}, \frac{\partial v}{\partial \sigma}\right) = \frac{D}{\rho_o K_m} (\tau_{sx}, \tau_{sy}), \omega = 0, \text{ at } \sigma = 0 \quad (6)$$

and

$$\left(\frac{\partial u}{\partial \sigma}, \frac{\partial v}{\partial \sigma}\right) = \frac{D}{\rho_o K_m} (\tau_{bx}, \tau_{by}), \omega = 0, \text{ at } \sigma = -1, \quad (7)$$

where  $(\tau_{sx}, \tau_{sy})$  and  $(\tau_{bx}, \tau_{by}) = C_d \sqrt{u^2 + v^2} (u, v)$  are the  $x$  and  $y$  components of surface wind and bottom stresses. The drag coefficient  $C_d$  is determined by matching a logarithmic bottom layer to the model at a height  $z_{ab}$  above the bottom, i.e.,

$$C_d = \max\left(k^2 / \ln\left(\frac{z_{ab}}{z_o}\right)^2, 0.0025\right), \quad (8)$$

where  $k = 0.4$  is the von Karman's constant and  $z_o$  is the bottom roughness parameter.

[9] The surface and bottom boundary conditions for temperature are:

$$\frac{\partial T}{\partial \sigma} = \frac{D}{\rho c_p K_h} [Q_n(x, y, t) - Q_s(x, y, 0, t)], \text{ at } \sigma = 0, \quad (9)$$

$$\frac{\partial T}{\partial \sigma} = \frac{A_H D \tan \alpha}{K_h + A_H \tan^2 \alpha} \frac{\partial T}{\partial n}, \text{ at } \sigma = -1, \quad (10)$$

where  $Q_n(x, y, t)$  is the net surface heat flux;  $c_p$  is the specific heat of seawater.  $A_H$  is the horizontal thermal diffusivity,  $\alpha$  is the bottom inclination angle and  $n$  is the horizontal coordinate on the  $\sigma$  surface in the direction of the bottom slope as defined in Figure A1 (Appendix A).  $Q_s(x, y, 0, t)$  is the shortwave flux incident at sea surface given as

$$Q_s(x, y, z, t) = Q_s(x, y, 0, t) [R e^{-az} + (1 - R) e^{-bz}], \quad (11)$$

where  $a$  and  $b$  are attenuation lengths for longer and shorter (blue-green) wavelength components of the shortwave irradiance, and  $R$  is the percent of the total flux associated with the longer-wavelength irradiance. This absorption profile, first suggested by Kraus [1972], has been used in numerical studies of upper ocean diurnal heating by Simpson and Dickey [1981a, 1981b] and others. The absorption of downward irradiance is included in the temperature (heat) equation in the form of

$$\begin{aligned} \hat{H}(x, y, z, t) &= \frac{\partial Q_s(x, y, \sigma, t)}{D \partial \sigma} \\ &= \frac{Q_s(x, y, 0, t)}{D \rho c_p} \left[ \frac{R}{a} e^{\frac{\sigma D + \zeta}{a}} + \frac{1 - R}{b} e^{\frac{\sigma D + \zeta}{b}} \right]. \end{aligned} \quad (12)$$

This approach leads to a more accurate prediction of near-surface temperature than the flux formulation based on a single wavelength approximation [Chen et al., 2003b].

[10] The surface and bottom boundary conditions for salinity are:

$$\frac{\partial S}{\partial \sigma} = \frac{S(\hat{P} - \hat{E})D}{K_h \rho}, \text{ at } \sigma = 0, \quad (13)$$

$$\frac{\partial S}{\partial \sigma} = \frac{A_H D \tan \alpha}{K_h + A_H \tan^2 \alpha} \frac{\partial S}{\partial n}, \text{ at } \sigma = -1, \quad (14)$$

where  $\hat{P}$  and  $\hat{E}$  are precipitation and evaporation rates, respectively. Note that a groundwater flux can be easily added into the model by modifying the bottom boundary conditions for vertical velocity and salinity.

## 2.1. POM

[11] POM is a structured grid, finite difference model that consists of external and internal modes and is solved numerically using two split time steps [Blumberg and Mellor, 1987]. The external mode is composed of the vertically integrated transport equations of (1) and (2). The transport equations are solved for the sea surface elevation  $\zeta$  by an explicit difference scheme in which the time step  $\Delta t_1$  is constrained by  $\min(\Delta x, \Delta y) / \sqrt{gD}$ , where  $\Delta x$  and  $\Delta y$  are the horizontal grid sizes. The internal mode is a fully 3-D model described by equations (1)–(5) and solved using a longer time step  $\Delta t_2$  that is constrained by the phase speed of the lowest mode internal wave. Linkage between external and internal modes is through  $\zeta$ : the surface pressure gradients at each  $\Delta t_2$  time step in the internal mode are calculated directly by output of  $\zeta$  from the external mode.

[12] POM uses the curvilinear orthogonal transformation to fit moderately irregular coastal geometry. The equations are discretized following the design of an ‘‘Arakawa-C’’ grid and transport forms of equations are numerically solved using a second-order accurate central difference scheme. A time-filtering program is used to suppress the computational mode. Notice here that the bottom boundary conditions (10) and (14) for temperature and salinity in POM are simplified to  $\frac{\partial T}{\partial \sigma} = \frac{\partial S}{\partial \sigma} = 0$ . One reason for this is the difficulty in the finite difference method to calculate accurately  $\alpha$  and  $\frac{\partial T}{\partial n}$  over an irregular 3-D bottom slope. The error caused by inaccurate calculation of these two terms in a finite difference approach can be larger than their real values. This simplification is generally sound for most continental shelves where bottom slope and bottom topography are small. However, over a steep sloping bottom like the shelf break and continental slope, this simplification may overestimate vertical mixing in the bottom boundary layer and thus cause a numerical bias in horizontal and vertical velocities.

## 2.2. ECOM-si

[13] ECOM-si is the modified semi-implicit version of POM [Blumberg, 1994]. Treating both the barotropic pressure gradient in the momentum equations and water transport terms in the continuity equation implicitly, this model is solved numerically only with a single time step  $\Delta t$ . The

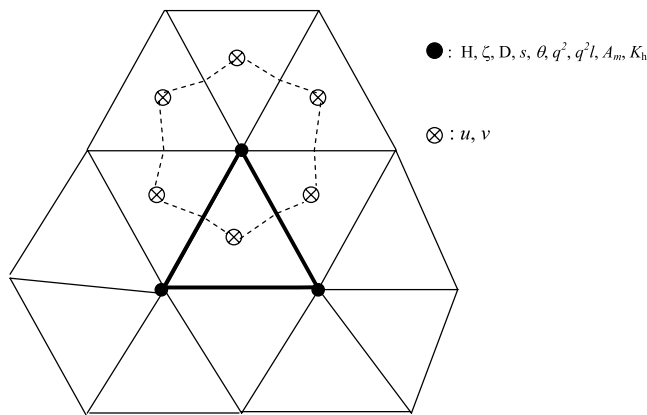


**Figure 1.** Locations of velocity and tracer variables in the unstructured grid of FVCOM.

semi-implicit numerical method used in ECOM-si leads to a linear symmetrical diagonal algebraic system at each time step, which can be solved efficiently by a preconditioned conjugate method with no sacrifice in computational time [Casulli, 1990]. In ECOM-si,  $\Delta t$  is constrained by  $\min(\Delta x, \Delta y)/\sqrt{u^2 + v^2}$ , which can be one order of magnitude larger than that chosen in POM for the same model problem. Increasing  $\Delta t$  must be balanced by the decrease in energy conservation due to the numerical decay nature of semi-implicit schemes.

[14] The curvilinear transformation in ECOM-si has recently been replaced by a nonorthogonal transformation developed by Chen *et al.* [2004a]. In this new modified code, the nonlinear advection terms in momentum, temperature, and salinity equations are calculated using the multidimensional positive definite advection transport algorithm [Smolarkiewicz, 1984; Smolarkiewicz and Clark, 1986]. To avoid numerical instability due to the Euler forward scheme for the case with no advection and horizontal and vertical diffusions [Mesinger and Arakawa, 1976], a predicted corrector scheme is adopted to compute the Coriolis terms in the momentum equation [Chen *et al.*, 2001a; Zhu *et al.*, 2001]. Unlike POM, ECOM-si (both orthogonal and nonorthogonal coordinate versions) does not include a time filter program to ensure computational stability. However, ECOM-si also uses the same simplified bottom boundary conditions for temperature and salinity ( $\frac{\partial T}{\partial \sigma} = \frac{\partial S}{\partial \sigma} = 0$ ) as POM, which does not satisfy the no flux condition over a sloping bottom (see Appendix A).

### 2.3. FVCOM

[15] FVCOM is an unstructured grid, finite volume, 3-D primitive equation coastal ocean model developed recently by Chen *et al.* [2003a, 2004b]. Like POM, FVCOM also is composed of external and internal modes that are computed separately using two split time steps. A distinct difference is that FVCOM is solved numerically by the flux calculation in an integral form of the equations (1)–(5) over nonoverlapping, unstructured triangular grids. Flux calculation ensures not only the conservation of total mass over the whole computational domain but also on individual meshes used to compute currents and water properties. The finite volume numerical approach combines the advantages of

finite element methods for geometric flexibility and finite difference methods for simple discrete code structure and computational efficiency. Since FVCOM was recently developed, a brief discussion on the grid configuration is given below.

[16] FVCOM subdivides the horizontal numerical computational domain into a set of nonoverlapping unstructured triangular meshes. An unstructured triangle is composed of three nodes, a centroid, and three sides (Figure 1), on which  $u$  and  $v$  are placed at centroids and all scalar variables, such as  $\zeta$ ,  $H$ ,  $D$ ,  $\omega$ ,  $S$ ,  $T$ ,  $\rho$ ,  $K_m$ ,  $K_h$ ,  $A_m$ , and  $A_h$  are placed at nodes. Scalar variables at each node are determined by the net flux through the sections linked to centroids and the middle point of the sideline in the surrounding triangles (the tracer control element (TCE)), while  $u$  and  $v$  at centroids are calculated on the basis of the net flux through three sides of that triangle (the momentum control element (MCE)). A second-order accuracy upwind finite difference scheme is used for flux calculation in the integral form of the advective terms [Kobayashi *et al.*, 1999; Hubbard, 1999], and the modified fourth-order Runge-Kutta time-stepping scheme is used for time integration. Similar to ECOM-si, no temporal/spatial smoothing is needed for numerical stability.

[17] Unlike POM and ECOM-si, FVCOM uses an exact form of the no flux bottom boundary conditions for temperature (10) and for salinity (14). The bottom slope and gradients of temperature and salinity over each TCE on 3-D irregular bottom topography in FVCOM can be calculated using a simple Green's theorem (see Appendix A). This finite volume approach ensures the correct physics of the bottom boundary layer over a sloping bottom, which is found to be essential in simulating mixing and upwelling over abrupt bottom slopes and submarine banks.

## 3. Model Validation

### 3.1. Wind-Induced Surface Gravity Waves in a Circular Lake

[18] The first example used to validate FVCOM is a comparison with POM and ECOM-si regarding the simulation of wind-induced long-surface gravity waves in an idealized circular lake for which an analytic solution can be derived. Two types of geometries are considered: both flat bottom and sloping bottom lakes. Discussion for each case is given below.

#### 3.1.1. Flat Bottom Case

[19] For a constant surface wind stress imposed in the surface in the  $x$  direction on the flat bottom circular lake shown in Figure 2, the inviscid linear transport process in a polar coordinate system satisfies the following governing equations:

$$\frac{\partial U}{\partial t} - fV = -gH \frac{\partial \zeta}{\partial r} + \tau_{ax} \cos \theta, \quad (15)$$

$$\frac{\partial V}{\partial t} + fU = -gH \frac{\partial \zeta}{r \partial \theta} - \tau_{ax} \sin \theta, \quad (16)$$

$$\frac{\partial \zeta}{\partial t} + \frac{1}{r} \left( \frac{\partial V}{\partial \theta} + \frac{\partial rU}{\partial r} \right) = 0, \quad (17)$$

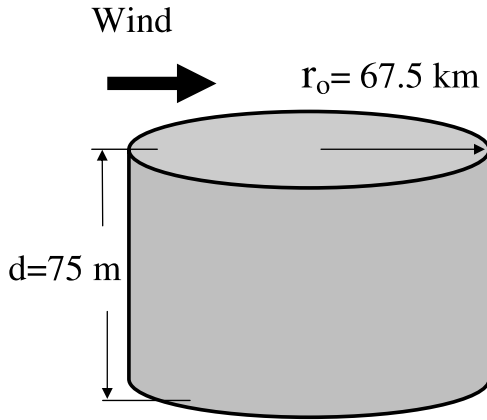


**Figure 2.** Idealized circular lake configuration.

where  $r$  and  $\theta$  are the radius and angle axes;  $U$  and  $V$  are the  $r$  and  $\theta$  components of volume transport;  $\zeta$  is the surface elevation;  $f$  and  $g$  are the Coriolis parameter and gravitational acceleration;  $H$  is the mean water depth; and  $\tau_{ax}$  is the  $x$  (eastward) component of the surface wind stress.

[20] Assuming that the lake is initially at rest, the motion is continuous in the interior, and there is no flux into the solid boundary, the boundary and initial conditions for (15)–(17) are given as

$$U|_{r=r_0} = 0; (U, V, \zeta)|_{r=0} \rightarrow \text{finite}, \quad (18)$$

$$(U, V, \zeta)|_{t=0} = 0. \quad (19)$$

Equations (15)–(17) with conditions (18) and (19) can be solved analytically [Csanady, 1968; Birchfield, 1969], with the exact solution in nondimensional variables  $\zeta$ ,  $U$  and  $V$  given as

$$\zeta(r, \theta, t) = \frac{\tau_o}{\lambda^4} \left[ A_o(r) \cos \theta + \sum_{k=1}^{\infty} a_k A_k(r) \cos(\theta - \hat{\sigma}_k t) \right] \quad (20)$$

$$U(r, \theta, t) = \frac{\tau_o}{\lambda^3} \left[ \left( \frac{A_o(r)}{r} - 1 \right) \sin \theta - \sum_{k=1}^{\infty} b_k F_k(r) \sin(\theta - \hat{\sigma}_k t) \right] \quad (21)$$

$$V(r, \theta, t) = \frac{\tau_o}{\lambda^3} \left[ \left( \frac{dA_o(r)}{dr} - 1 \right) \cos \theta - \sum_{k=1}^{\infty} b_k G_k(r) \cos(\theta - \hat{\sigma}_k t) \right] \quad (22)$$

where  $\lambda = \frac{c}{r_o f}$ ;  $c = \sqrt{gH}$ ;  $\tau_o = \frac{\tau_{ax} g}{r_o^2 f^2}$ ;  $a_k = (\hat{\sigma}_k - 1)/(\hat{\sigma}_k + 1 - \hat{\sigma}_k^2/\lambda^2)$ ,  $b_k = a_k/(\hat{\sigma}_k^2 - 1)$ . The parameters  $A_o(r)$ ,  $A_k(r)$ ,  $F_k(r)$  and  $G_k(r)$  are given as

$$A_o(r) = I_1(r/\lambda)/I_1(1/\lambda); \quad (23)$$

$$A_k(r) = \begin{cases} I_1(\gamma_k r)/I_1(\gamma_k) |\hat{\sigma}_k| < 1; \\ J_1(\gamma_k r)/J_1(\gamma_k) |\hat{\sigma}_k| > 1; \end{cases} \quad (24)$$

$$F_k(r) = A_k(r)/r - \hat{\sigma}_k(dA_k(r)/dr); \quad (25)$$

$$G_k(r) = dA_k/dr - \hat{\sigma}_k A_k(r)/r; \quad (26)$$

where  $\gamma_k^2 = (1 - \hat{\sigma}_k^2)/\lambda^2$ ;  $J_1$  and  $I_1$  are the original and modified first-kind Bessel functions, respectively. The  $k$ th mode frequency  $\hat{\sigma}_k$  is determined by solving the following equation:

$$1 - \sigma_k \gamma_k \frac{1}{I_1(\gamma_k)} \frac{dI_1(\gamma_k)}{d\gamma_k} = 0. \quad (27)$$

[21] The solutions (20)–(22) consist of two parts: one is a wind-induced steady state motion, and the other is the Kelvin/Poincare waves excited at  $t = 0$ . Amplitudes of the surface elevation and velocity decrease rapidly as mode number increases; the exact solutions of  $\zeta$ ,  $U$  and  $V$  can be accurately expressed by a sum of the first 7 modes with frequencies of  $\hat{\sigma}_{1,2,3,\dots,7} = 7.0; -7.84; 21.41; -21.48; 34.3; -34.33; \text{ and } -47.03$ .

[22] Considering a case with  $f = 10^{-4}$  /s,  $r_o = 67.5$  km,  $H = 75$  m,  $c = 27.1$  m/s and  $\lambda = 4.016$ , we compared FVCOM with POM and ECOM-si versus the exact solution of (20)–(22). Numerical grid for FVCOM was constructed using nonoverlapping triangular meshes with a horizontal resolution of about 1.78 km (Figure 3, top). Total number of grid cells was 9084. Numerical grids for POM and ECOM-si were made using square cells with the same horizontal resolution as FVCOM (Figure 3, bottom). The total number of cells was 5776, 4536 of which were used for computation. The time step was 15 s for FVCOM and POM and 1 s for ECOM-si. The stability criteria is  $\Delta t < \Delta s/\sqrt{gH}$  for POM and FVCOM and  $\Delta t < \Delta s/|u|$  (where  $\Delta s$  is the horizontal resolution and  $|u|$  is the magnitude of the current velocity) for ECOM-si, respectively. While a longer time step could be selected in principle for ECOM-si, the ECOM-si derived surface elevation and transports computed using the same time step as FVCOM and POM decreased rapidly with time because of the decay nature of the semi-implicit scheme used in ECOM-si. A shorter time step of 1 s was required for ECOM-si to provide an identical result to POM. A comparison of computational efficiency between ECOM-si and POM should be made with caution, because stability does not always represent accuracy.

[23] Numerical experiments were conducted for three cases with constant eastward surface winds of 3, 5, and 10 m/s. The resulting surface wind stresses for these three cases were 0.013, 0.036, and 0.144 N/m<sup>2</sup>. In the case with a wind speed of 3 m/s, for example, the FVCOM-computed surface elevation and transport accurately matched the analytical solutions in both amplitudes and phases. POM showed a phase delay after one model hour. The time delay in phase increased with model hours: 17.5 minutes at the end of the first model day and then up to 68.4 minutes at the end of the fourth model day (Figure 4 and Table 1). POM-induced time-dependent phase shift can be seen clearly in Figure 5. With a time step of 1 s, ECOM-si showed the exact same results as POM.

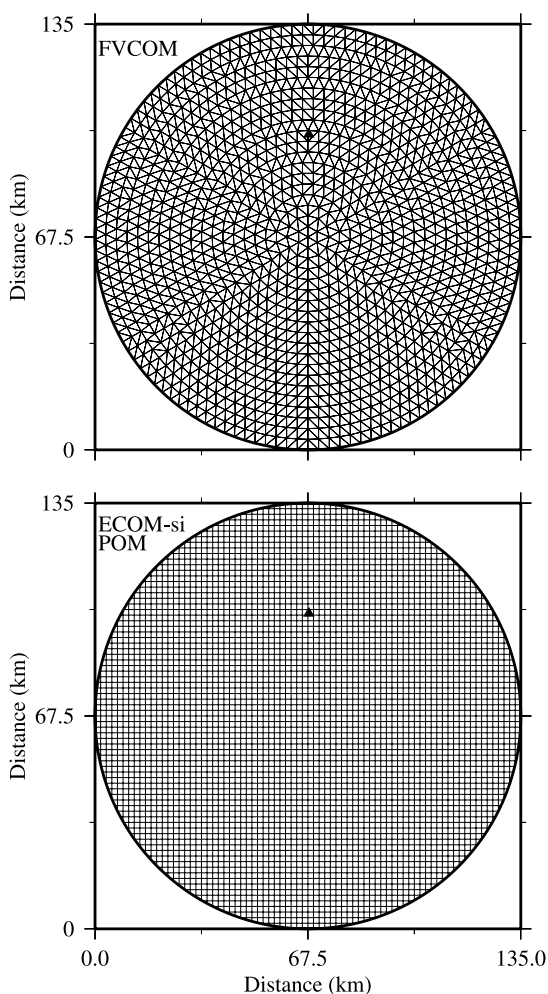


**Figure 3.** Unstructured and structured grids used in FVCOM and POM/ECOM-si, respectively, for the wind-induced gravity wave test in the idealized circular lake shown in Figure 2. The triangular symbol ( $x = 67.5$  km,  $y = 101.25$  km) is the location used for the comparison of surface elevation and transport between analytic, FVCOM, POM, and ECOM-si solutions.

[24] The time delay in phases of model-computed elevation and transport found in POM and ECOM-si is clearly related to the rectangular grid used in the model, which failed to resolve accurately the coastline of the circular lake. This phase delay decreased with an increase of the horizontal resolution (Table 1). For example, as the cell number for POM or ECOM-si was doubled (i.e.,  $\Delta x = \Delta y \approx 0.89$  km), the time delay in the phases of elevation and transport decreased to 8.3 minutes at the end of the first model day and to 36.3 minutes at the end of the fourth model day, about one-half those reported in the case with  $\Delta x = \Delta y \approx 1.78$ . Even better agreement in amplitude and phase between POM or ECOM-si and the analytical solution was found when  $\Delta x = \Delta y \approx 0.45$  km. While the phase delay should approach zero as horizontal resolution increases to a certain level, this approach sacrifices computational efficiency. The time required for a 10-day run of POM increased 4 times when  $\Delta x(\Delta y)$  was reduced from 1.78 km to 0.89 km, and

18 times when  $\Delta x(\Delta y)$  was reduced to 0.45 km. Even for  $\Delta x(\Delta y) < 0.45$  km, the phase delay in POM-computed elevation and transport still exists!

[25] Unlike POM or ECOM-si, FVCOM seemed less sensitive to horizontal resolution. When the length of a triangular sideline increased to 2.67 km (twice as large as that shown above), FVCOM caused little shift in phase, even though the model led to minor underestimation of amplitudes of the elevation and transport. Therefore with regard to computational efficiency, the unstructured grid seems better than the structured grid to capture the correct physics and reach a certain accuracy of numerical simulation in this case for the wind-induced motion in a flat-bottomed circular lake.

### 3.1.2. Sloping Bottom Case

[26] Considering now a circular lake with water depth given as

$$H(r) = H_o \left[ 1 - \left( \frac{r}{r_o} \right)^2 \right], \quad (28)$$

where  $r_o$  is the radius of the lake and  $H_o$  is the water depth at the center (Figure 6). *Birchfield and Hickie* (BH) [1977] found an analytic solution for equations of (15)–(17) with boundary conditions (18)–(19) for this geometry and a constant wind stress. The exact solution of the surface elevation and transport for the case with  $H_o = 100$  m and  $r_o = 100$  km is in the form of a complicated double series, in which each radial mode number contains three wave terms: two for a gravity wave pair and one for a topographic wave. By carefully examining the solution, we found that the series does not converge in the first few leading modes. As an initial value problem, the analytical solution is dominated by the first four radial modes in the first model day, while higher modes must be taken into account for a longer time period. For this reason, the comparison of the numerical models with the analytical solution was limited here to the first model day. FVCOM, POM, and ECOM-si use the  $\sigma$ -coordinate transformation in the vertical which becomes invalid as  $H(r_o) = 0$ . In order to make these models run for this case, a depth of 0.5 m was added everywhere in  $H(r)$ , with the understanding that the numerical solution might lead to a bias with BH's analytical solution for a longtime run.

[27] In the first model day, both FVCOM and POM produced a reasonable simulation of the elevation composed of the first four radial modes of the analytical solution, although POM showed a small perturbation at the center at the first model hour and a biased maximum value away from the coast at the 20th hour (Figure 7). Significant difference between FVCOM and POM occurred after day two. For example, at the end of day five, FVCOM with a horizontal resolution of 5 km showed a symmetric distribution of elevation over the circular lake, with a maximum positive value on the right coast and a minimum negative value on the left coast (Figure 8a). Although POM with a horizontal resolution of 2.5 km showed a similar pattern, multiple artificial eddies occurred in the transition region from positive elevation to negative elevation and a series of small-scale perturbations in elevation appeared along the coast on both sides of the wall (Figure 8b). This difference

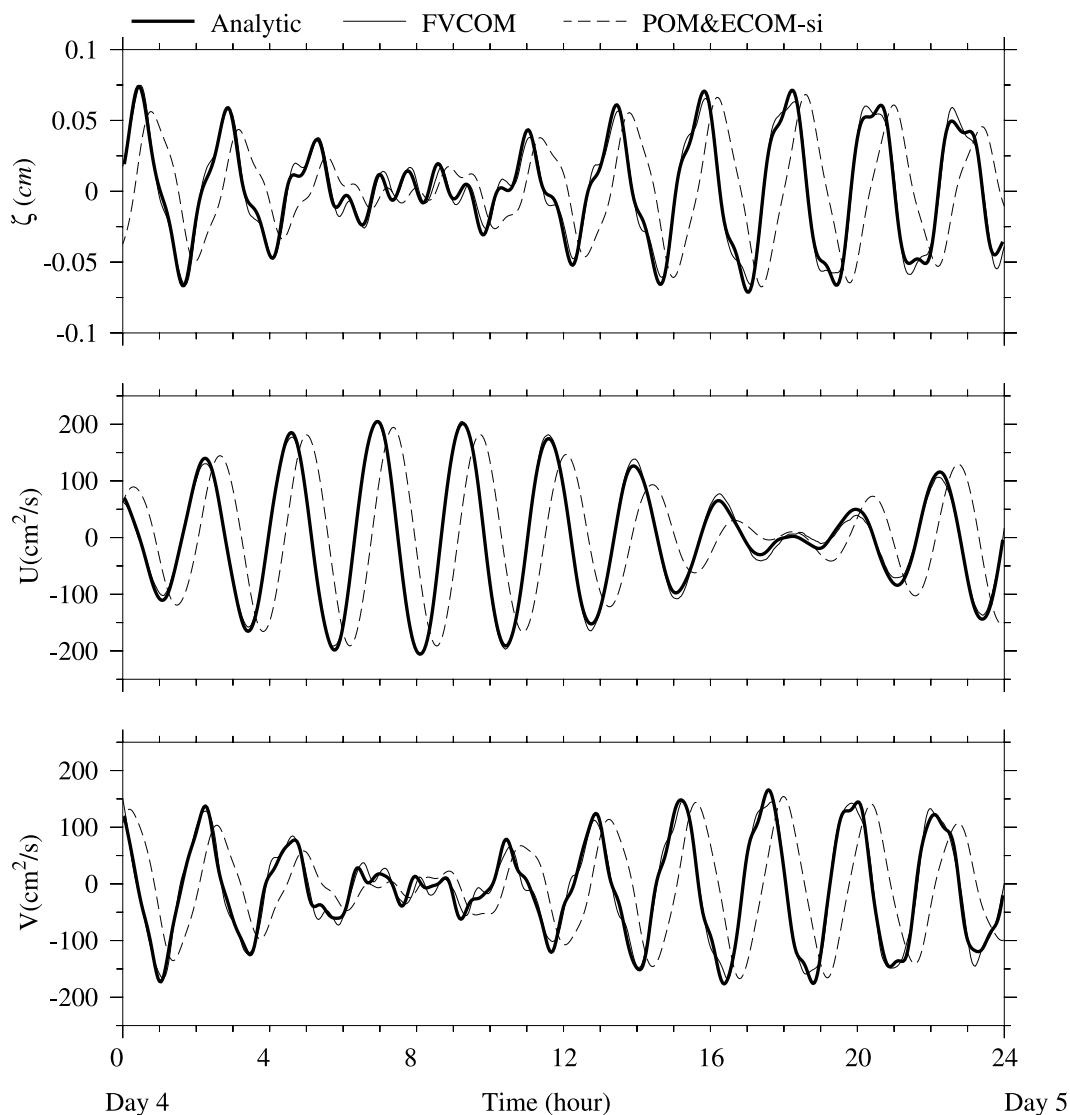


**Figure 4.** Comparison of time series of surface elevation ( $\zeta$ ),  $x$ -component ( $U$ ), and  $y$ -component ( $V$ ) transports between analytic (heavy solid line), FVCOM (thin solid line), and POM/ECOM-si (dashed line) solutions at the location shown in Figure 3.

was clearly evident in model-computed transport. FVCOM showed a spiral circulation along the coast and a double cell circulation in the interior (Figure 9a), while POM-computed circulation was characterized by multiple eddies in the transition region of elevation and significant divergence flows close to the coast (Figure 9b). It is clear that eddies predicted by POM are numerical noise due to inaccurate fitting of the curved coastline of the circular lake, since the size and strength of these eddies decreased as horizontal resolution increased (Figure 10). Again, this numerical noise should disappear as horizontal resolution increases but only with a large sacrifice in computational efficiency. The noise may reduce if the no-slip boundary condition is used at the boundary.

### 3.2. Tidal Resonance in a Semienclosed Basin

[28] On the basis of the results of tidal simulation in the Bohai Sea, *Chen et al.* [2003a] found that FVCOM succeeded in capturing the near-resonance nature of the  $M_2$

tidal wave in semienclosed bays in the Bohai Sea, while ECOM-si failed. Numerical experiments with FVCOM and ECOM-si for tidal simulation raises the question on the importance of resolving accurately the coastal geometry for near-resonance tidal waves in coastal oceans. To address

**Table 1.** Relationship Between Phase Delay and Horizontal Resolution for an Idealized Circular Lake Experiment With POM<sup>a</sup>

$\Delta s$ , km	$\Delta t$ , s	$T_h$ , hours	$\Delta$ phase, min			
			1 day	2 days	3 days	4 days
1.78	15	2	17.5	29.8	48.1	68.4
0.89	15	8	8.3	14.0	17.9	36.3
0.44	2	36	2.5	5.9	7.8	8.2

<sup>a</sup> $\Delta s$  is the horizontal resolution;  $\Delta t$  is the time step used for time integration;  $T_h$  is the total compute times for a 10 day integration on a Dec Alpha 600 MHz Workstation;  $\Delta$  phase is the phase delay relative to the analytical solution.

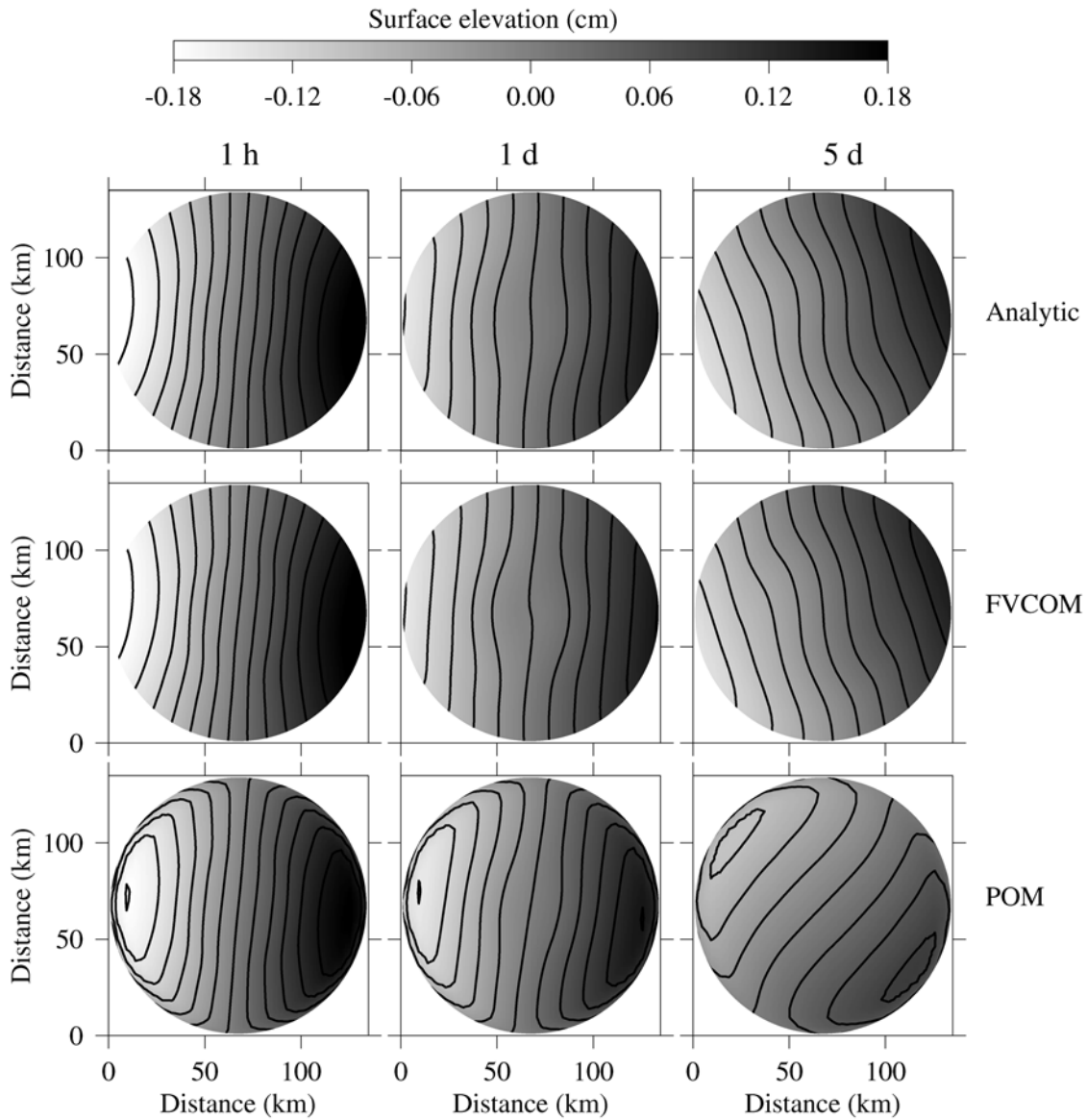


**Figure 5.** Comparison of the surface elevation at the end of the 1st hour, 1st day, and 5th day between analytic, FVCOM, and POM/ECOM-si solutions.

this question, we applied FVCOM, POM, and ECOM-si to idealized semienclosed rectangular and sector channels to examine the response of these models to tidal forcing at the open boundary under normal (nonresonance) and near-resonance conditions.

**3.2.1. One-Dimensional Case: A Rectangular Channel**

[29] The geometric structure of the channel is shown in Figure 11, where  $H(x) = xH_o/L$  is the water depth that decreases linearly toward the end of the channel,  $H_o$  is the water depth of the open boundary of the channel,  $L_1$  and  $L$  are the distances from the origin to the end and mouth of the channel, and  $B$  is the width of the channel. Considering a 2-D nonrotating initial value problem, the governing equations controlling tidal waves in the channel are given as

$$\frac{\partial u}{\partial t} + g \frac{\partial \zeta}{\partial x} = 0; \quad \frac{\partial \zeta}{\partial t} + \frac{\partial u H}{\partial x} = 0. \tag{29}$$

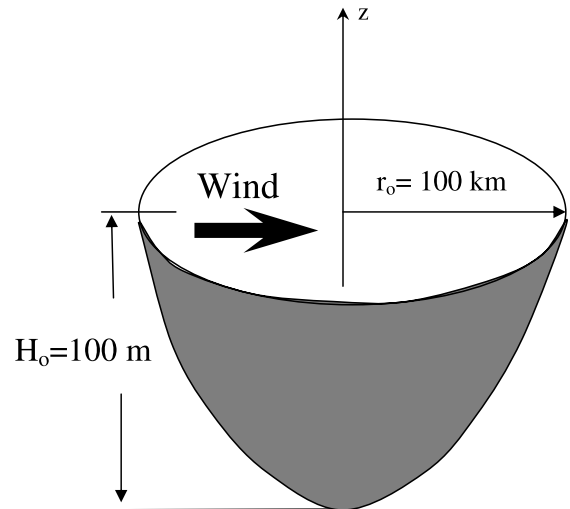


**Figure 6.** The circular lake with sloping bottom configuration.

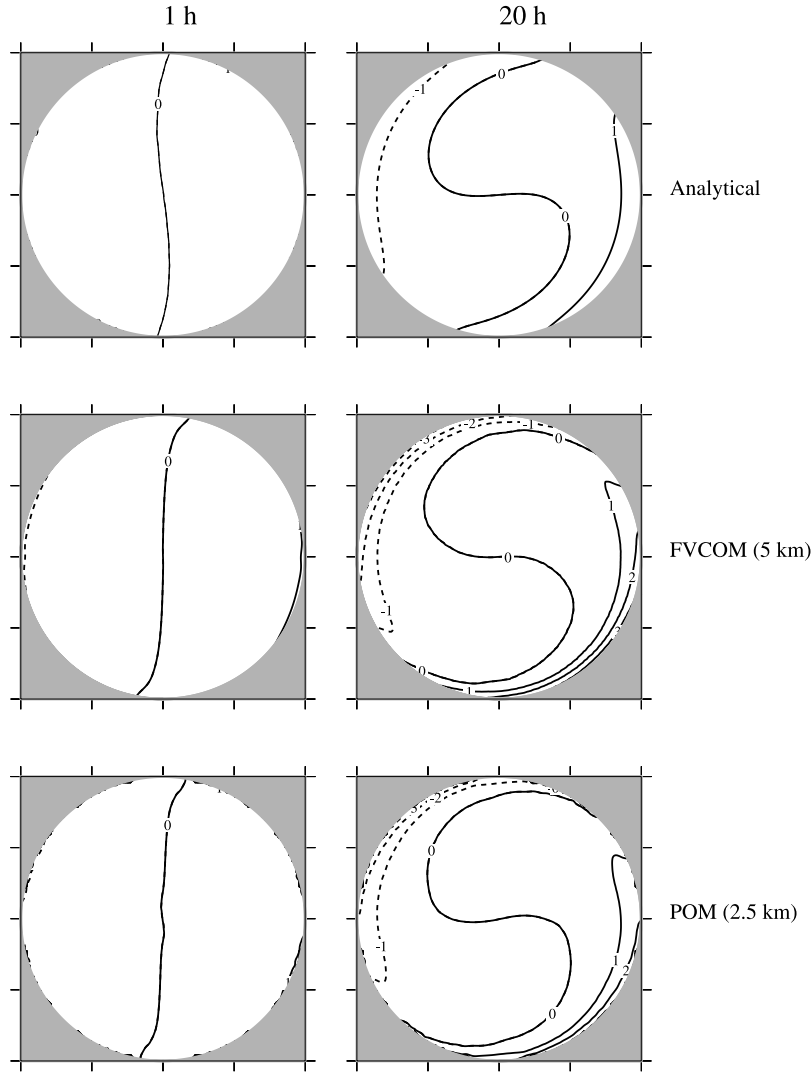


**Figure 7.** Comparison of surface elevation at the end of the 1st and 20th hours between analytic, FVCOM, and POM solutions. Horizontal resolution is 5 km for FVCOM and 2.5 km for POM.

Rewriting  $\zeta = \zeta_o e^{-i\sigma t}$ ,  $u = u_o e^{-i\sigma t}$  and substituting them into (29) yields,

$$\frac{d^2 \zeta_o}{dx^2} + \frac{1}{x} \frac{d\zeta_o}{dx} + \frac{1}{x} \frac{L\sigma^2}{gH_o} \zeta_o = 0. \quad (30)$$

Specifying a periodic tidal forcing with amplitude  $A$  at the mouth of the channel, i.e.,

$$\zeta_o|_{x=L} = A, \quad (31)$$

and a no-flux boundary condition at the end of the channel, i.e.,

$$\left. \frac{d\zeta_o}{dx} \right|_{x=L_1} = 0, \quad (32)$$

the analytical solution of (30) is given as

$$\zeta_o = \frac{A}{F(L, L_1, k)} [Y'_o(2k\sqrt{L_1})J_o(2k\sqrt{x}) - J'_o(2k\sqrt{L_1})Y_o(2k\sqrt{x})] \quad (33)$$

where

$$F(L, L_1, k) = J_o(2k\sqrt{L})Y'_o(2k\sqrt{L_1}) - Y_o(2k\sqrt{L})J'_o(2k\sqrt{L_1}), \quad (34)$$

$J_o$  and  $Y_o$  are the zeroth-order Bessel functions of the first and second kinds, and

$$k^2 = \frac{\sigma^2 L}{gH_o}. \quad (35)$$

[30] For geometric parameter values of  $B = 5$  km (note: while this is a simple 1-D case with the solution independent of  $B$ , a finite ( $>0$ ) value of  $B$  is chosen here to allow use of the 3-D models for this 1-D study),  $H_o = 20$  m,  $L - L_1 = 290$  km, and a periodic tidal forcing with an  $M_2$  tidal frequency  $\sigma = 2\pi/(12.42 \times 3600)$  s, two cases are considered in the numerical experiments. In the first case,  $L = 580$  km,  $L_1 = 290$  km, and  $H(L_1) = 10$  m. For a given small tidal

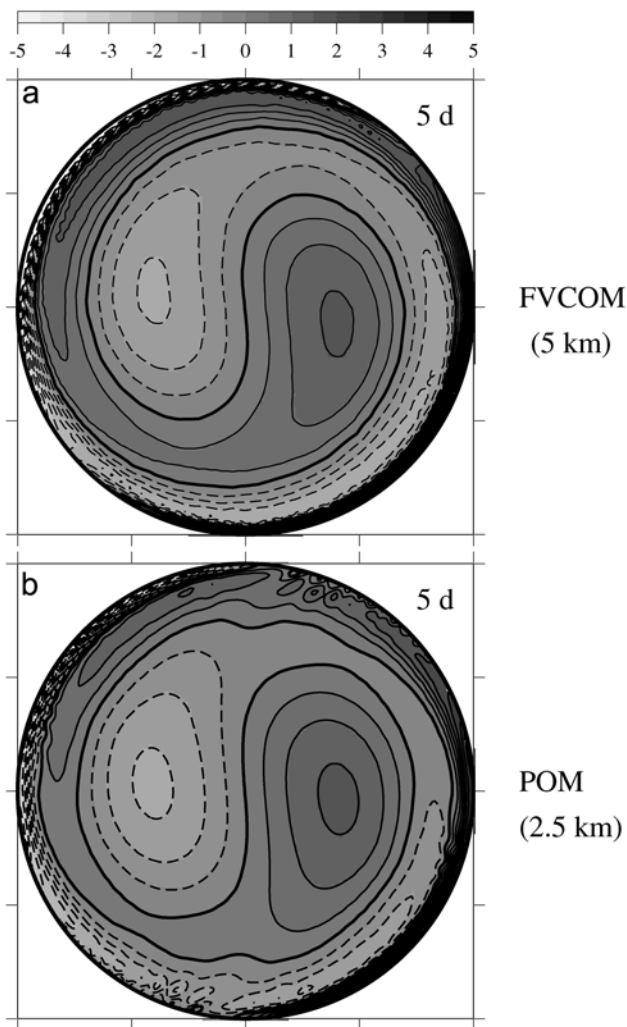


**Figure 8.** Comparison of FVCOM and POM surface elevations at the end of the 5th day. Horizontal resolution is 5 km for FVCOM and 2.5 km for POM.

amplitude of 1 cm at the mouth of the channel,  $\zeta_o$  is characterized with a node point at the middle of the channel and a maximum value of 1.2 cm at the end of the channel (Figure 12, solid line). This case is far from resonance. In the second case,  $L = 300$  km,  $L_1 = 10$  km,  $H(L_1) = 0.67$  m and the channel is very close to resonance. For the same given tidal forcing at the channel mouth,  $\zeta_o$  reaches a maximum elevation exceeding 20 cm at the end of the channel and a node point at a distance of 65 km away from the end (Figure 13, solid line). For the sake of discussion, here we refer to the first and second cases as “normal” and “near-resonance” cases, respectively.

[31] Numerical experiments were designed for a 2-D rectangular channel in which nonlinear advection, cross-channel variation, rotation, and mixing were set to zero. The FVCOM and POM/ECOM-si numerical grids were constructed by triangular and square meshes with a horizontal resolution of 2.5 km. Since the cross-channel current was zero everywhere, only two triangular and square grid cells

in the cross-channel section were needed to calculate water elevation and along-channel transport for either FVCOM or POM/ECOM-si. To avoid artificial oscillations caused by an impulse of tidal forcing at open boundary, the elevation and current at each grid at the initial time step were specified according to the analytical solution.

[32] For both normal and near-resonance cases, the amplitudes and phases of the  $M_2$  tidal wave computed by FVCOM, POM, and ECOM-si were almost identical, with all of them in close agreement with the analytical solution (Figures 12 and 13). The analytic solution describes a standing wave with a node point either at the center (for the normal case) or near the coast (for the near-resonance case) of the channel. These features were accurately reproduced by all the three models no matter which numerical schemes were used.

[33] This result indicates that in this 1-D linear case, with a proper selection of time step and horizontal resolution, the numerical solution of the tidal resonance did not depend on the numerical methods used to solve the governing equations. The standard version of POM uses a second-order

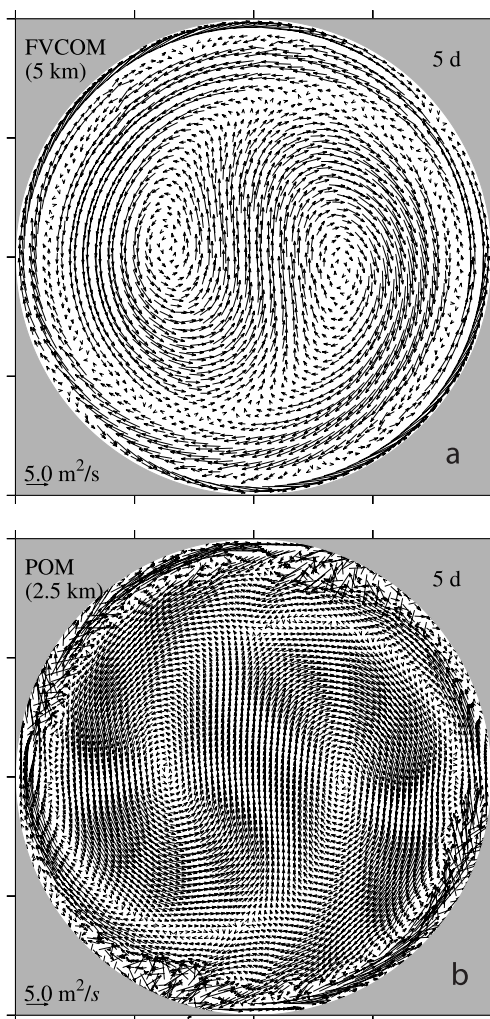


**Figure 9.** Comparison of FVCOM and POM horizontal transport vector fields at the end of the 5th day. Horizontal resolution is 5 km for FVCOM and 2.5 km for POM.

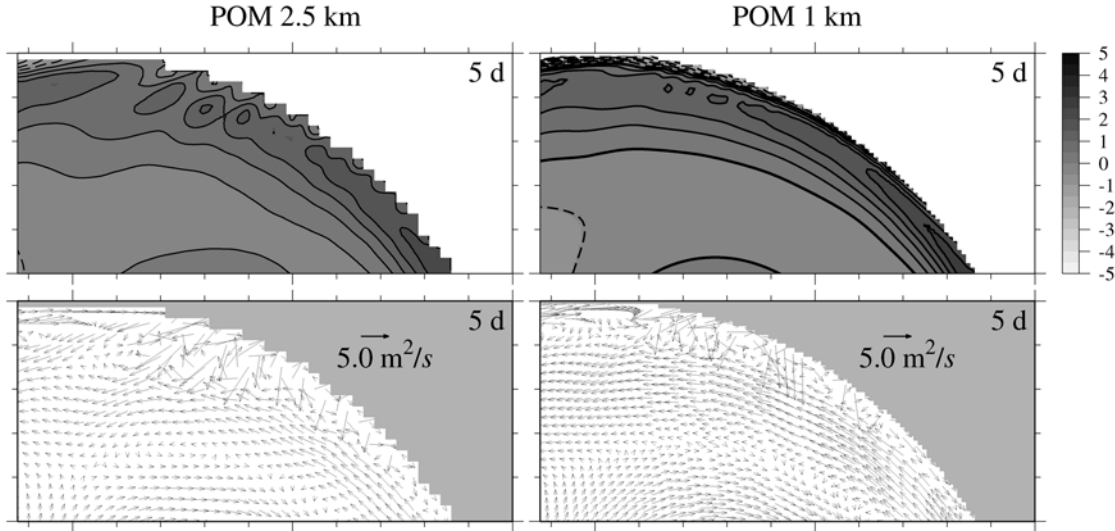


**Figure 10.** Comparison of surface elevation and horizontal transport vector fields in the sea level transition zone at the 5th day for POM cases with horizontal resolutions of 1.0 and 2.5 km.

accurate central difference scheme for both time integration and spatial gradients of surface elevation and volume transport. Although it requires a time filter to avoid numerical instability, the filter seems to work well in the 1-D rectangular case. ECOM-si uses a semi-implicit scheme to remove the restriction of the time step used to calculate the surface gravity waves. By selecting the time step with caution, this method also resolves tidal resonance with the same accuracy as POM. FVCOM is solved numerically using an integrated form of the momentum equations with an approach of flux calculation with a second-order accurate upwind scheme for advection and the modified fourth-order Runge-Kutta time stepping for time integration [Chen *et al.*, 2003a]. The result of FVCOM was identical to POM and ECOM-si.

### 3.2.2. Two-dimensional Case: A Sector Channel

[34] Consider a 2-D nonrotating initial value problem of the tidal oscillation in a semienclosed, constant depth sector channel shown in Figure 14. The governing equations controlling the boundary-forced tidal waves in this case are given as

$$\frac{\partial V_r}{\partial t} = -g \frac{\partial \zeta}{\partial r}, \quad (36)$$

$$\frac{\partial V_\theta}{\partial t} = -g \frac{\partial \zeta}{r \partial \theta}, \quad (37)$$

$$\frac{\partial \zeta}{\partial t} + \frac{\partial r V_r H_0}{r \partial r} + \frac{\partial V_\theta H_0}{r \partial \theta} = 0, \quad (38)$$

where  $r$  and  $\theta$  are the radius and angle axes;  $H_0$  is the constant mean water depth;  $V_r$  and  $V_\theta$  are the  $r$  and  $\theta$  components of velocity; and  $\zeta$  is the surface water elevation.

[35] Eliminating  $V_r$  and  $V_\theta$  from (36)–(38) yields an equation for  $\zeta$  as follows

$$\frac{\partial^2 \zeta}{\partial t^2} - g H_0 \nabla^2 \zeta = \frac{\partial^2 \zeta}{\partial t^2} - g H_0 \left( \frac{\partial^2 \zeta}{\partial r^2} + \frac{1}{r} \frac{\partial \zeta}{\partial r} + \frac{1}{r^2} \frac{\partial^2 \zeta}{\partial \theta^2} \right) = 0. \quad (39)$$

[36] Assuming  $\zeta = \text{Re}[\zeta_0(r, \theta) e^{-i(\omega t - 90^\circ)}]$  and substituting it into (39) produces

$$\frac{\partial^2 \zeta_0}{\partial r^2} + \frac{1}{r} \frac{\partial \zeta_0}{\partial r} + \frac{1}{r^2} \frac{\partial^2 \zeta_0}{\partial \theta^2} + \frac{\omega^2}{g H_0} \zeta_0 = 0. \quad (40)$$

On the solid wall, the boundary conditions of no normal flux are given as

$$\left. \frac{\partial \zeta_0}{\partial r} \right|_{r=L_1} = 0; \quad \left. \frac{\partial \zeta_0}{\partial \theta} \right|_{\theta=\alpha/2} = 0; \quad \left. \frac{\partial \zeta_0}{\partial \theta} \right|_{\theta=-\alpha/2} = 0, \quad (41)$$

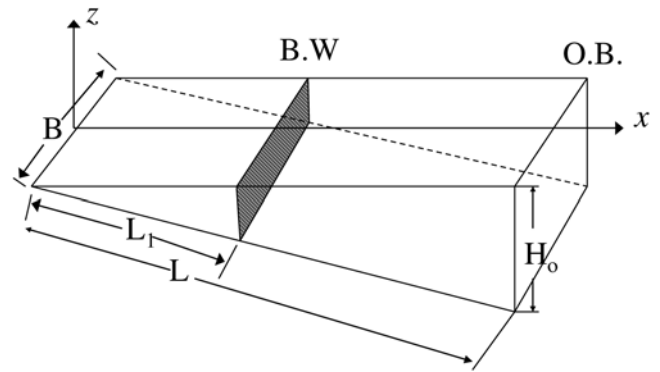


**Figure 11.** Configuration of the semienclosed channel for the tidal wave test case. O.B.: open boundary; B.W.: boundary wall at the end of the channel; B: the width of the channel; and  $H_0$ : the mean depth at the open boundary.  $L_1$  and  $L$ : the distance of the boundary wall and open boundary from the origin  $x = 0$ .

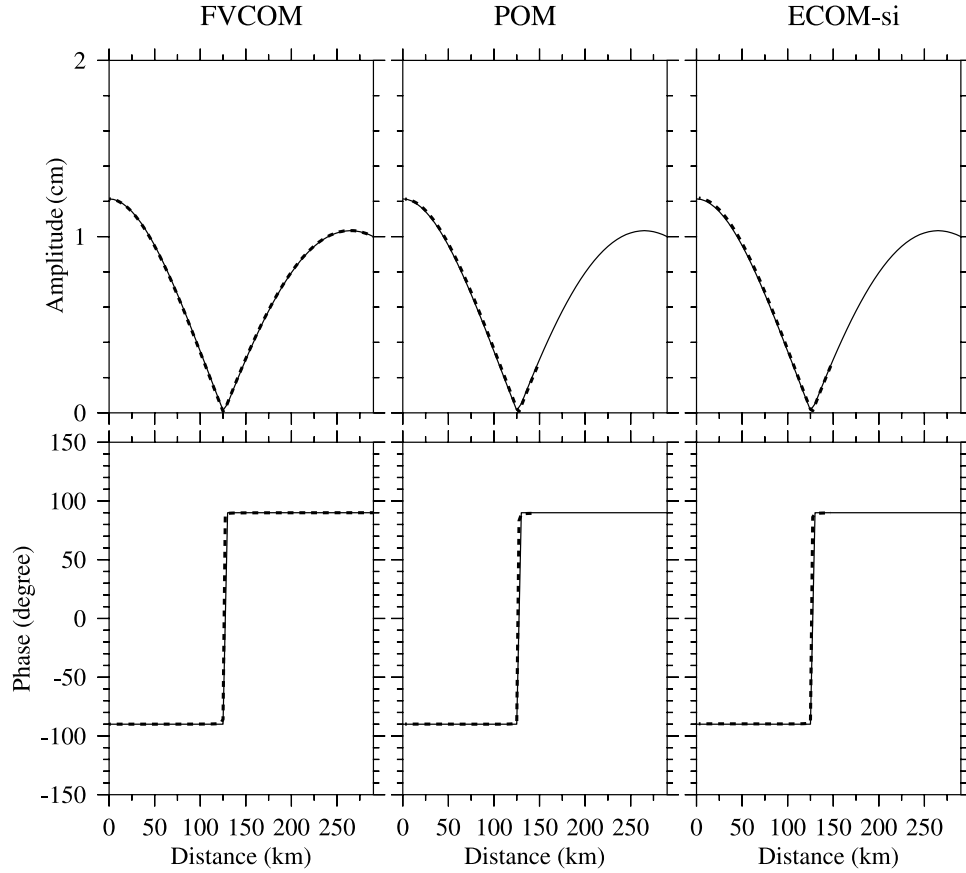


**Figure 12.** Comparison of model-predicted and analytic amplitudes and phases in the along-channel direction for the nonresonance case. (solid line) Analytic solution; (dashed line) model simulation. The origin of the horizontal coordinate is located at the end of the channel. In this case the initial distributions of current and surface elevation are specified using the analytic solution.

where  $\alpha$  is the arc angle of the sector that is a measure of the width. Specifying a harmonic tidal forcing at the open boundary given as

$$\zeta_0|_{r=L} = \bar{A} \cos \left[ m\pi \left( \theta + \frac{\alpha}{2} \right) / \alpha \right], \quad (42)$$

the analytic solution of (40) satisfying (41) is given as

$$\zeta_0(r, \theta) = \left[ c_1 J_{\gamma_m} \left( r \frac{\omega}{\sqrt{gH_0}} \right) + c_2 Y_{\gamma_m} \left( r \frac{\omega}{\sqrt{gH_0}} \right) \right] \cdot \cos \left[ \frac{m\pi(\theta + \alpha/2)}{\alpha} \right] \quad (43)$$

where

$$c_1 = \bar{A} \cdot Y'_{\gamma_m} \left( L_1 \frac{\omega}{\sqrt{gH_0}} \right) / \left[ J_{\gamma_m} \left( L \frac{\omega}{\sqrt{gH_0}} \right) Y'_{\gamma_m} \left( L_1 \frac{\omega}{\sqrt{gH_0}} \right) - J'_{\gamma_m} \left( L_1 \frac{\omega}{\sqrt{gH_0}} \right) Y_{\gamma_m} \left( L \frac{\omega}{\sqrt{gH_0}} \right) \right]$$

$$c_2 = -\bar{A} \cdot J'_{\gamma_m} \left( L_1 \frac{\omega}{\sqrt{gH_0}} \right) / \left[ J_{\gamma_m} \left( L \frac{\omega}{\sqrt{gH_0}} \right) Y'_{\gamma_m} \left( L_1 \frac{\omega}{\sqrt{gH_0}} \right) - J'_{\gamma_m} \left( L_1 \frac{\omega}{\sqrt{gH_0}} \right) Y_{\gamma_m} \left( L \frac{\omega}{\sqrt{gH_0}} \right) \right]$$

$$\gamma_m = m\pi/\alpha.$$

$J_{\gamma_m}$  and  $Y_{\gamma_m}$  are the  $\gamma_m$ th-order Bessel functions of the first and the second kind, respectively.

[37] For geometric parameter values of  $H_0 = 1$  m,  $\alpha = \pi/4$ ,  $L_1 = 90$  km,  $m = 1$ , and a periodic  $M_2$  tidal forcing [ $\omega = 2\pi/(12.42 \times 3600$  s)], two cases were considered in numerical experiments. The first case is referred to the “normal” case with  $L = 132$  km and  $\bar{A} = 1$  cm. In this case,  $\zeta(r, \theta, t)$  is characterized by an oscillation with symmetric amplitudes relative to a node line at  $\theta = 0$ . The oscillation on either side of the node is  $90^\circ$  out of phase, with the maximum amplitude of 1.5 cm appearing at the lateral solid boundary. The second case is referred to “near-resonance” case, in which the tidal forcing was the same as that in the first case but  $L = 158$  km. In this case, the oscillation pattern is the same as that in the “normal” case but  $\zeta(r, \theta, t)$  has a maximum amplitude at the lateral boundary exceeding 48 cm, which is about 32 times larger than that observed in the “normal” case.

[38] In both cases, FVCOM was configured using the unstructured triangular grid with a horizontal resolution of about 2 km (Figure 15, top). To examine the influence of coastal geometric fitting on the numerical solution, we ran POM and ECOM-si using curvilinear and rectangular grids with horizontal resolutions of 1 and 2 km, respectively (Figure 15, middle and bottom).

[39] In the “normal” case, POM and ECOM-si with the curvilinear grid produced nearly identical results as FVCOM,

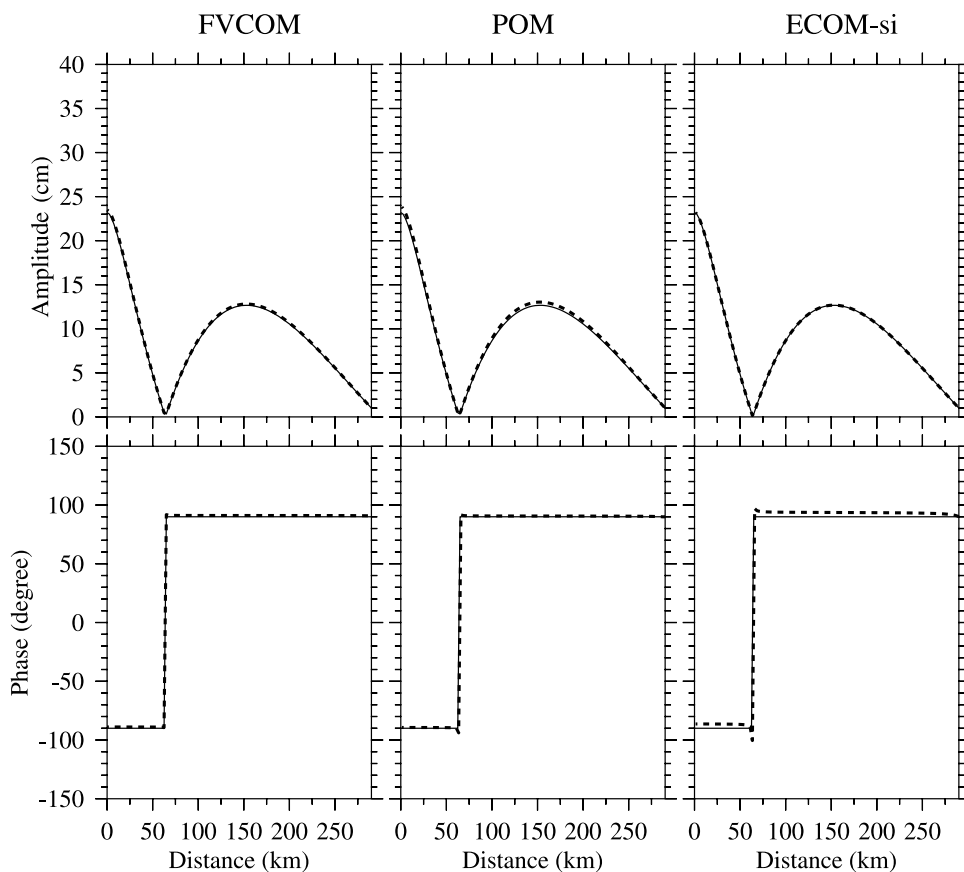


**Figure 13.** Comparison of model-predicted and analytic amplitudes and phases in the along-channel direction for the near-resonance case. (solid line) Analytic solution; (dashed line) model simulation. The origin of the horizontal coordinate is located at the end of the channel. In this case the initial distributions of current and surface elevation are specified using the analytic solution.

accurately matching the analytic solution (Figure 16). Even for the rectangular grid case, POM still produced a reasonable numerical solution with small errors of  $\sim 0.1$  cm in amplitude and  $\sim 0.5^\circ$  in phase. In this case, ECOM-si was very similar to POM, except with a small error in phase. These results suggest that in the “normal” case, the mismatch of coastal geometry due to the rectangular grid is only an issue regarding accuracy. This issue can be easily addressed by increasing the horizontal resolution.

[40] In the “near-resonance” case, FVCOM accurately reproduced the amplitude and phase of the large oscillation (Figure 17, left), while POM and ECOM-si were sensitive to grid structure and horizontal resolution. For the curvilinear grid case, POM-derived amplitude of the oscillation along the line A–B (see Figure 14) decayed with time in the case with 2-km horizontal resolution, but it converged closely to the analytic solution as the horizontal resolution was increased to 1 km (Figure 17, middle). In this case, the convergence of ECOM-si to the analytic solution was much smaller than POM. Even for the case with a horizontal resolution of 1 km, ECOM-si still showed a considerable, time-dependent decay in amplitude and a bias in phase along the line A–B. For the rectangular grid case, POM- and ECOM-si-derived oscillation amplitudes in the case with 2-km horizontal resolution increased with tidal cycles, which led to numerical instability when the amplitude of the

surface elevation was larger than the water depth after 30 tidal cycles. With the horizontal resolution increased to 1 km, POM and ECOM-si reached stable numerical resolutions. At the end of the 20th tidal cycle, both POM and

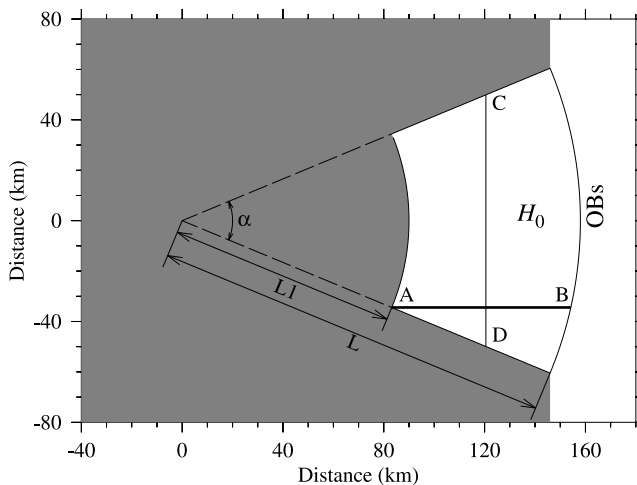


**Figure 14.** Configuration of the idealized semienclosed sector channel. Lines A–B and C–D are transects used to make comparison of amplitude and phase for the different model runs.

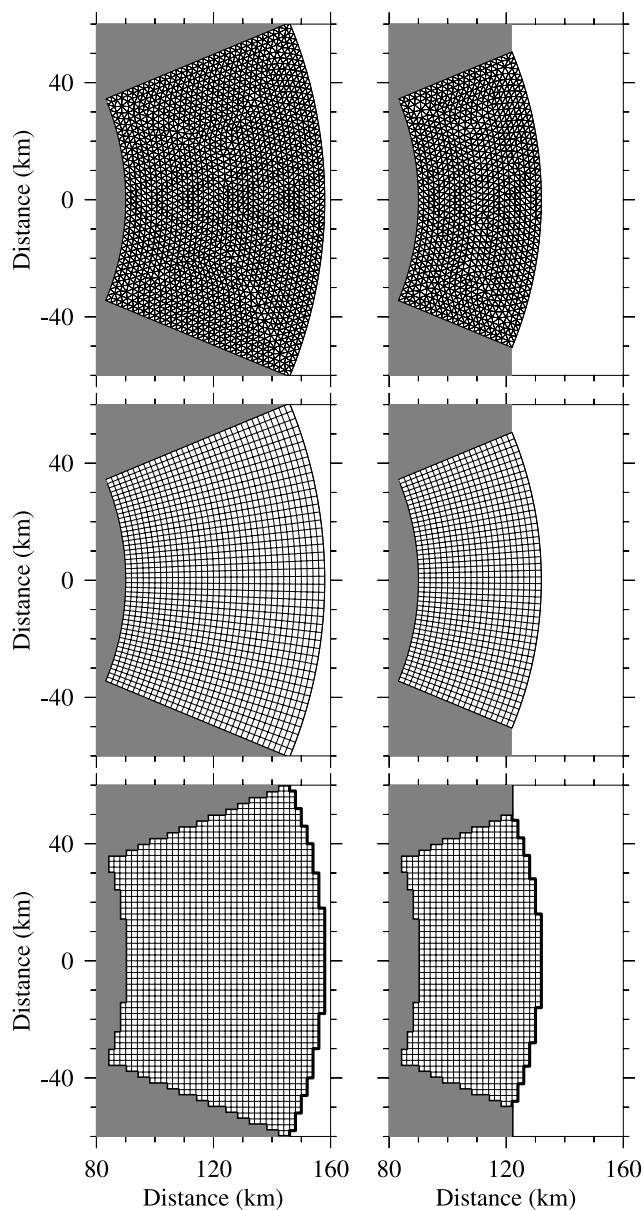


**Figure 15.** Unstructured and structured grids used in FVCOM and POM/ECOM-si, respectively, for the tidal experiments in the semienclosed sector channel shown in Figure 13. Nonoverlapped triangular grid with a horizontal resolution of about 2 km is used for FVCOM. POM and ECOM-si are configured using curvilinear (middle) and rectangular (bottom) grids with horizontal resolutions of 1 and 2 km, respectively (only the 2-km grids are shown here).

ECOM-si captured the spatial distribution of the amplitude of the oscillation, but caused an unrealistic bias in phase (Figure 18). With the increase of time integration, POM showed an oscillatory numerical solution relative to the analytical solution in both amplitude and phase (Figure 19). Increasing the horizontal resolution in POM and ECOM-si improved the accuracy in amplitude, but did not help in eliminating the big bias in phase. This experiment suggests that when the tidal oscillation is close to resonance, the phase

of the oscillation is much more sensitive to geometrical fitting than the amplitude.

### 3.3. Freshwater Discharge Over an Idealized Continental Shelf

[41] The dynamics of buoyancy-driven flow caused by freshwater discharge is a hot topic in coastal oceanography. Numerous studies have been conducted on this topic in the last decade, which have provided us with a comprehensive understanding of the mechanisms for the formation and evolution of the low-salinity plume or fronts over the continental shelf [e.g., *Chao, 1988; Chapman and Lentz, 1994; Kourafalou et al., 1996; Garvine, 1999; Chen et al., 1999; Chen, 2000*]. The discussion given below focuses solely on the comparison between FVCOM and POM for freshwater discharge experiments on idealized shelves in a circular lake.

#### 3.3.1. Cosine Shelf With a Curved Coastline

[42] Consider a closed circular lake with a shelf bottom profile given by

$$H(r) = \begin{cases} \frac{H_d + H_o}{2} + \frac{H_d - H_o}{2} \cos \left[ \frac{\pi(r - r_o)}{R - r_o} \right] & r_o \leq r \leq R \\ H_d & r < r_o \end{cases} \quad (44)$$

where  $H(r)$  is the water depth at distance  $r$  from the origin of the circle,  $R$  is the radius of the circular lake,  $r_o$  is the distance from the origin of the circle to the edge of the shelf,  $H_o$  is the water depth at  $R$ , and  $H_d$  is the constant water depth region of  $r \leq r_o$ . With a constant freshwater discharge of  $1000 \text{ m}^3/\text{s}$  injected into the lake from the mesh at the center point of the southern coast, we examined the influence of horizontal resolution and coastline geometric matching on the evolution of the coastal low-salinity plume that develops over the sloping shelf in the circular lake. The background salinity used in this experiment was a constant 30 practical salinity units (psu) throughout the domain.

[43] According to the theory of coastal low-salinity plumes, the freshwater injected into the shelf of the lake should rotate clockwise and then flow along the coast like a coastal trapped wave. A low-salinity plume or front should form because of mixing between the freshwater and shelf water. These basic dynamical features were all captured by POM and FVCOM, but the plume structure predicted by POM and FVCOM differed significantly because of the numerical schemes used to estimate tracer advection, horizontal resolution, and accuracy of geometric matching. For the case with a horizontal resolution of 4.22 km, the low-salinity plume predicted by FVCOM occupied the entire shelf with a cross-shelf scale the same as the width of the shelf, while the plume predicted by POM extended over the interior region off the shelf, forming a detached eddy-like circulation at the outer edge of the shelf by day 10 (Figures 20–22, top). When the horizontal grid size was reduced to 1.78 km, the plumes predicted by FVCOM and POM shifted toward the coast (Figures 20–22, middle). A quasi-equilibrium state occurred as the horizontal grid size was made smaller or equal to  $\sim 0.89 \text{ km}$  (Figures 20–22, bottom). These results provided two important facts. Firstly, attention must be paid to the horizontal resolution in simulating the spatial structure of the low-salinity plume over the inner shelf of the coastal ocean, no matter which model is used. Secondly, the finite

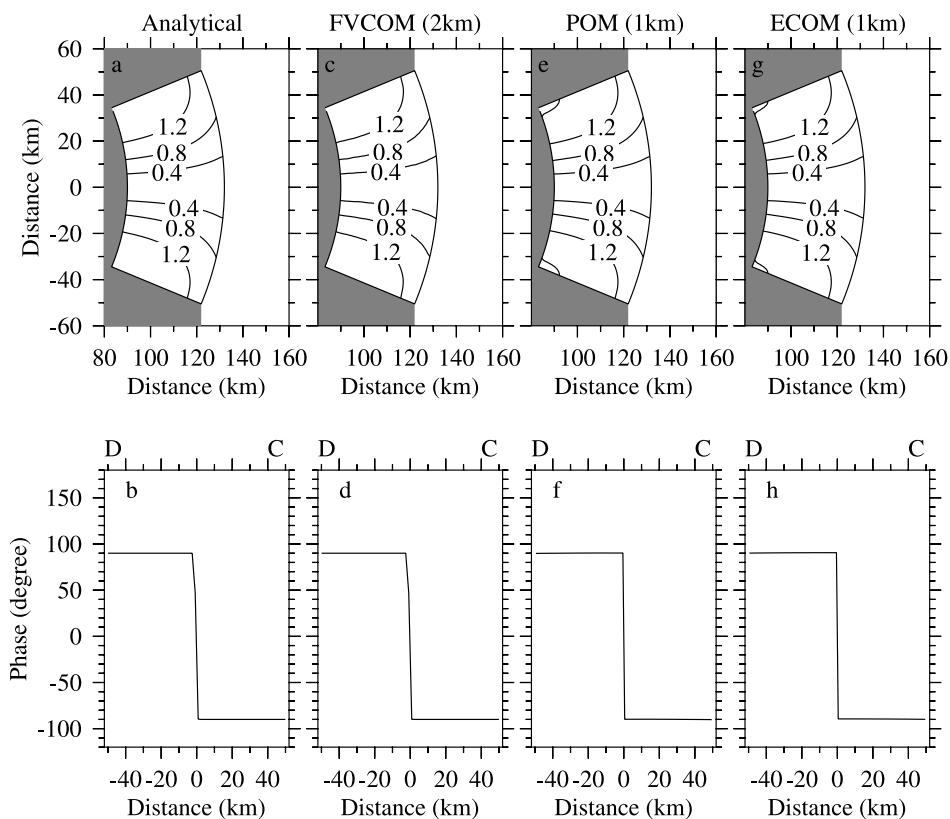


**Figure 16.** (top) Surface elevation amplitude (cm) and (bottom) phase ( $^{\circ}$ G) along the cross-sector (D–C) transect for analytic, FVCOM, POM, and ECOM-si solutions for the “normal” case.

difference model may lose the coastally trapped wave nature of the low-salinity plume at a certain lower horizontal resolution and thus produce an unrealistic, artificial eddy structure over the shelf.

[44] For a given horizontal resolution, the low-salinity plume propagated faster along the shelf in FVCOM than POM. This difference was caused by geometric matching of the curved coastline and the difference in tracer advection schemes. The unstructured triangular grid used in FVCOM provided accurate coastline matching with a guarantee of no mass flux through the coastal wall. Downstream of the freshwater source, the plume water predicted by FVCOM flowed along the curved coastline, with a maximum water level and along-shelf current at the coast (Figure 23, top). The square grids used in POM resulted in a step-like coastal boundary in the numerical computational domain. Since the no flux condition was applied in a direction normal to the step-shaped boundary, the maximum along-shelf current occurred at a distance away from the coast (Figure 23, bottom). This step-shaped coastal model boundary acted like a drag force to slow down the downstream movement of the low-salinity plume and to exaggerate the cross-shelf secondary current within the plume.

[45] POM also features a curvilinear orthogonal coordinate transformation, which could provide proper matching of smooth coastlines. While POM setup with polar coordinates for this circular lake case should give much better results that are comparable with FVCOM, in general, curvilinear orthogonal coordinate transformations are not as efficient as unstructured triangular grids in application to

real coastal ocean domains characterized with irregular geometry.

### 3.3.2. Impact of Horizontal Resolution on the Structure of the Plume

[46] In the above case, the tracer concentration at grid points of the freshwater runoff source in FVCOM and POM was specified. This approach seems very straightforward because the tracer concentration of the runoff is easily determined by direct measurements taken at either the river mouth or upstream. In the numerical model, this approach is built on an assumption that no mixing occurs in the individual computational volumes connected to the freshwater source (see Appendix B). This assumption should be generally sound in the case with sufficient horizontal resolution, but it might cause an unrealistic buoyancy gradient near the source of the runoff and thus exaggerate the spatial scale and propagation speed of the low-salinity plume in the case with coarse horizontal resolution. This is a common issue no matter what types of models are used. Here we use FVCOM as an example to derive a criterion required for a convergence numerical solution of the river plume problem. This criterion should be applied to other finite difference models.

[47] Considering a case with no vertical and horizontal diffusion, the vertical integral form of the salinity equation in FVCOM with river runoff is given as

$$\frac{\partial SD}{\partial t} = \left[ - \oint v_n S D ds + Q \hat{S}_o \right] / \Omega^s \quad (45)$$

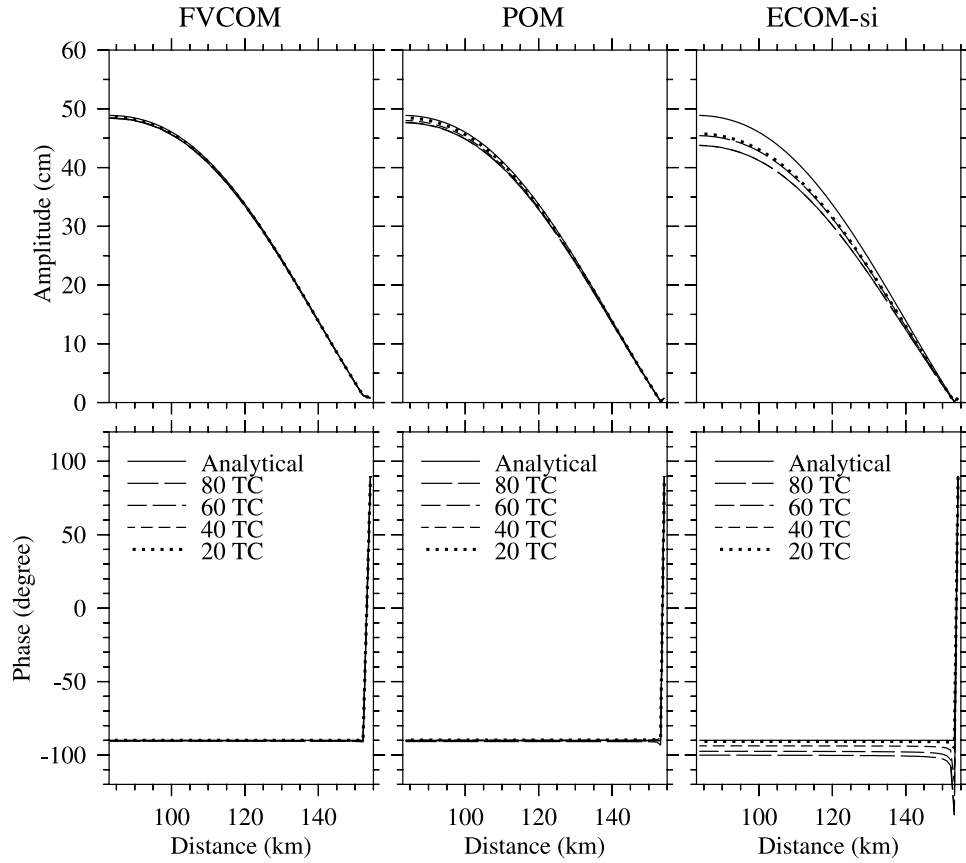


**Figure 17.** Comparisons between model-computed and analytic surface elevation amplitudes and phases along the transect A–B at the 20th, 40th, 60th, and 80th tidal cycles for the “near-resonance” case. (left) FVCOM; (middle) POM-curvilinear; and (right) ECOM-si curvilinear.

where  $S$  is the salinity at nodes of triangles connecting to the coastal node of the TCE,  $v_n$  is the depth-averaged velocity component normal to the boundary line of the TCE,  $Q$  is the volume transport of the runoff,  $\hat{S}_o$  is the salinity contained in the runoff water, and  $\Omega^\zeta$  is the area of the TCE containing the runoff. Assuming that at the time step  $n$ , the computational domain is filled with water with salinity of  $S^n$  that is uniform everywhere, then at time step  $n + 1$ , the salinity at the node point connected to the runoff source can be estimated by

$$S^{n+1} = S^n \left( \frac{D^n}{D^{n+1}} - \frac{\Delta t \oint v_n D^n ds}{D^{n+1} \Omega^\zeta} \right) + \frac{\Delta t Q \hat{S}_o}{D^{n+1} \Omega^\zeta}, \quad (46)$$

where  $\Delta t$  is the internal mode time step used for numerical computation. For simplification of scaling analysis, a forward numerical scheme is used here for time integration. Replacing the transform term in (46) using the continuity equation yields

$$S^{n+1} = S^n + \frac{\Delta t Q}{D^{n+1} \Omega^\zeta} (\hat{S}_o - S^n). \quad (47)$$

Specifying that  $\hat{S}_o = 0$  for the freshwater discharge case, (47) can be simplified to

$$S^{n+1} = \left( 1 - \frac{\Delta t Q}{D^{n+1} \Omega^\zeta} \right) S^n. \quad (48)$$

In order to keep  $S^{n+1}$  positive (i.e., the salinity can never become less than 0), (48) must satisfy

$$1 - \frac{\Delta t Q}{D^{n+1} \Omega^\zeta} \geq 0 \quad \text{or} \quad D^{n+1} \geq \frac{\Delta t Q}{\Omega^\zeta}. \quad (49)$$

Assuming that  $\Omega^\zeta \sim L^2$ ,  $\Delta t \sim I_{\text{split}} L / \sqrt{gD}$ ,  $D^{n+1} \sim D$ , where  $L$  and  $D$  are typical scales of the horizontal resolution of the TCE and water depth, then in order to ensure the salinity at the node point connected to the runoff to be zero, the magnitude of  $L$  must be

$$L \sim \frac{I_{\text{split}} Q}{D \sqrt{gD}}. \quad (50)$$

For given values of  $Q \sim 10^3 \text{ m}^3/\text{s}$ ,  $D \sim 10 \text{ m}$ , and  $I_{\text{split}} = 1$ ,  $L$  should be of order 100 m.

[48] In many numerical experiments for the coastal ocean, because of computer resource limitation,  $L$  is usually taken

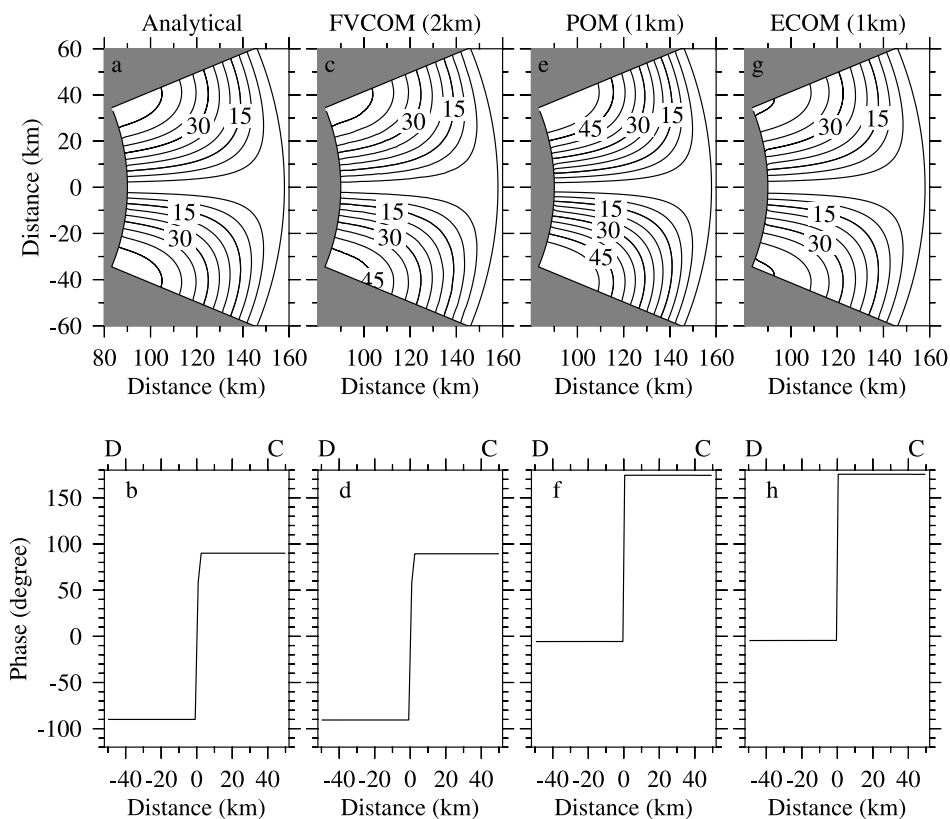


**Figure 18.** (top) Surface elevation amplitude (cm) and (bottom) phase ( $^{\circ}$ G) along the cross-sector (D–C) transect for the analytic, FVCOM, POM, and ECOM-si solutions at the 20th tidal cycle for the “near-resonance” case. In this case the exact solution shows the phase is opposite relative to the node line at  $\theta = 0$  with a large phase change in the radial direction near the open boundary. The cross-sector plot shown here is taken at the middle region of the channel.

as a value that is one order of magnitude larger than that required by the above criterion (50). This suggests that if we consider the mass conservation in the TCE connected to the runoff, the salinity calculated by (45) would be smaller than the salinity specified for the runoff water. On the other hand, if the horizontal resolution specified in the model is coarser than that required in (50), then, the model would not ensure mass conservation in the TCE that is connected to the runoff source and would also exaggerate the salinity gradient near the runoff source. Subsequently, it would overestimate the intensity of the low-salinity plume and cause an unrealistically faster propagation of the plume in the downstream direction.

[49] Consider an idealized continental shelf shown in Figure 24, with a water depth of 10 m at the coast, a linear slope of 0.0026 over the shelf, and a flat bottom in a region of 100 m deep. The background salinity is 30 psu. For a given discharge rate of  $1000 \text{ m}^3/\text{s}$ , the salinity at the node point connected to the runoff was estimated by two methods: one was specified as zero all the time, and the other was calculated directly in the TCE containing the runoff by the salinity equation. For the sake of discussion, we call here the first case “specified” and the second case “calculated”. For a given same river discharge, in the specified case, the river discharge does not affect the salinity balance in a TCE connected to the point source, while in the

calculated case, the salinity at the point source is determined by the salt equation with consideration of the mass balance.

[50] The spatial distributions and propagation speeds of the low-salinity plume predicted by the “specified” and “calculated” methods significantly differ in the case with a coarse horizontal resolution of 20 km (Figure 25, top). In the “specified” case, the zero salinity specified at the node point connected to the runoff source built a large salinity gradient. As a result, the edge of the plume had arrived in the downstream region about 300 km from the discharge source at day 10 (with an averaged speed of 35 cm/s). In the “calculated” case, however, since the salinity at the node point connected to the runoff source was calculated directly by the net salinity flux through the TCE, the salinity gradient was at least one order of magnitude smaller than that found in the “specified” case. As a result, the plume moved downstream at a slower speed of about 11 cm/s. It is clear that when horizontal resolution is low, the “specified” method tends to exaggerate the intensity and propagation of the plume, while the opposite results occurred in the “calculated” method.

[51] As horizontal resolution increases, the model-predicted plume tended to converge toward a similar pattern in either “calculated” and “specified” case (Figure 25, middle and bottom). The spatial distributions of the plume at day 10 predicted by these two methods were almost identical as the

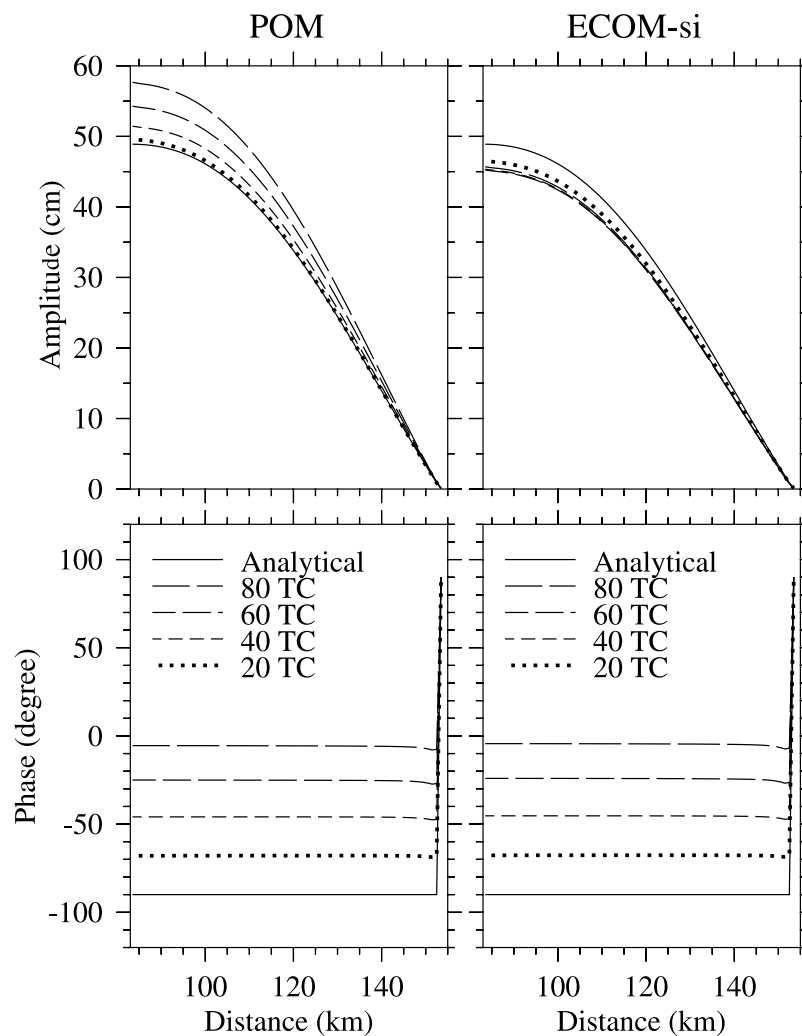


**Figure 19.** Comparisons between model-computed and analytic elevation amplitudes and phases along the A–B transect at the 20th, 40th, 60th, and 80th tidal cycles for the “near resonance” case. The results of POM and ECOM-si shown here are from runs using the rectangular grid (with a horizontal resolution of 1 km).

horizontal resolution reached 200 m. This is consistent with the conditions in criterion (50). If one agrees that 200 m is sufficient enough to produce the “true” structure of the plume in this case, then the “calculated” method seems to have a faster convergence rate than the “specified” method regarding the horizontal resolution required to produce this “true” structure. In the “calculated” case, the spatial distribution and propagation speed of the plume shown on day 10 in the case with 1-km horizontal resolution was very similar to the “true” one, while in the “specified” case, the spatial coverage of the plume predicted with 1-km horizontal resolution was still significantly larger than that shown in the “true” plume structure. This suggests that the “calculated” method is more practical than the “specified” method because it ensures salt conservation in the TCE connected to the runoff source and is also more flexible for horizontal resolution.

### 3.4. Thermal Boundary Layer on Steep Slope Bottom

[52] When a model with the  $\sigma$ -transformation coordinate system is applied to a shallow bank or shelf break, it faces

difficulty because of  $\sigma$ -errors over steep sloping bottoms. In the  $\sigma$ -transformation coordinate system, the baroclinic pressure gradient force is divided into two terms in each of the horizontal momentum equations. These two terms have the same order of magnitude but opposite signs. Small numerical errors in the calculation of these two terms can result in significant numerical biases of model-predicted current and density. Since the steep sloping bottom is a region where a rapid change of the thickness of  $\sigma$ -levels occurs, it is a region with the largest  $\sigma$ -errors [Haney, 1991; Mellor *et al.*, 1994; Chen and Beardsley, 1995; Song and Wright, 1998].

[53] The  $\sigma$ -errors in POM and ECOM-si have been examined both theoretically and numerically by Mellor *et al.* [1994] and Chen and Beardsley [1995]. Mellor *et al.* pointed out that these errors in POM can be contained at a certain level if sufficiently high horizontal and vertical resolution is used. Chen and Beardsley found that at a fixed location over a sloping bottom,  $\sigma$ -errors in ECOM-si increase with water depth. Since the buoyancy-driven velocity error caused by the  $\sigma$ -transformation always opposes the velocity in the thermal boundary layer on the sloping

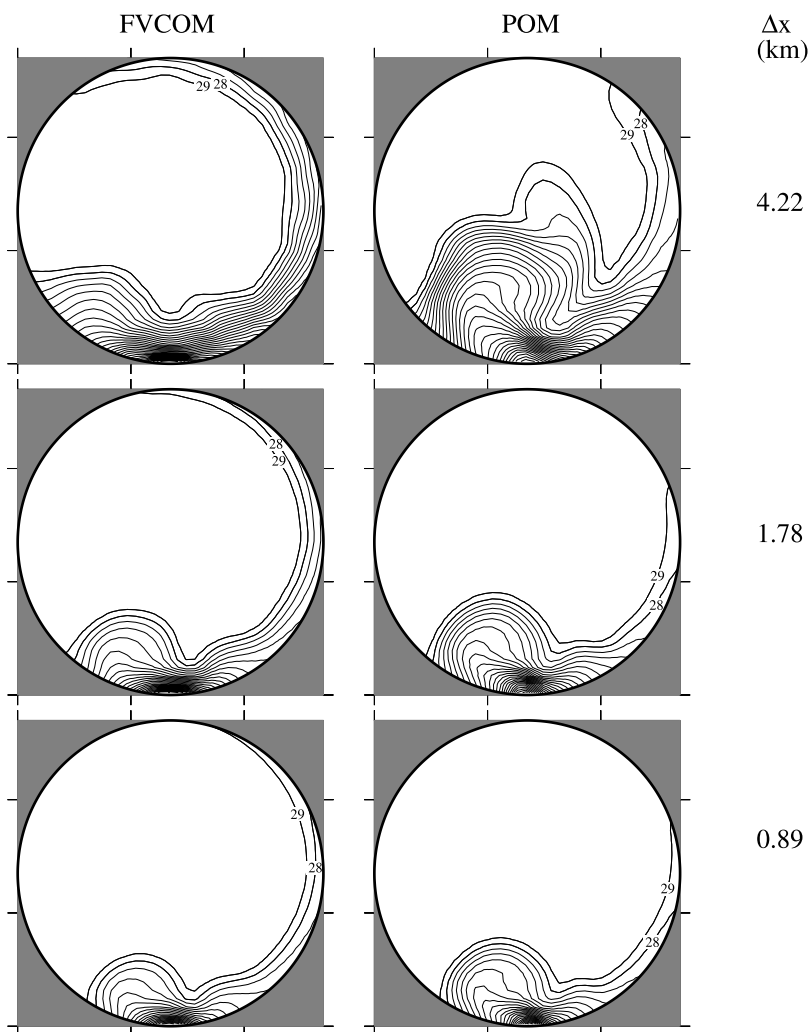


**Figure 20.** Comparison of FVCOM and POM surface salinity structures at the end of the 10th model day for runs with horizontal resolutions of 4.22, 1.78, and 0.89 km. In this case a constant freshwater discharge of  $1000 \text{ m}^3/\text{s}$  was specified at the central coastal TCE on the southern coast.

bottom, this error can be suppressed if the vertical resolution is high enough to resolve the thermal current near the bottom. FVCOM also uses the  $\sigma$ -transformation in the vertical so that its solutions should include similar  $\sigma$ -errors over steeply sloping bottoms. To investigate this problem, numerical experiments were conducted to compare FVCOM with POM for an idealized linear stratification case with background mixing over steep bottom topography.

[54] Consider a circular lake with a maximum radius of 78 km at the surface and maximum water depth of 300 m in the interior. This lake is characterized with a narrow circular shelf with a width of 15 km and a constant slope of 0.02. The slope specified in this study features steep bottom topography typically found near the shelf break or on banks (such as Georges Bank). The initial water temperature is assumed to be at linearly distributed in the vertical as

$$T = T_s - \frac{T_b - T_s}{H}, \quad (51)$$

where  $T_s$  is the surface water temperature taken as  $15^\circ\text{C}$ ,  $T_b$  is the bottom water temperature given as  $6^\circ\text{C}$ , and  $H$  is the maximum water depth specified as 300 m.

[55] POM uses the specified temperature bottom condition  $\frac{\partial T}{\partial z} = 0$ , while FVCOM uses the complete temperature bottom condition given in (10). To compare FVCOM with POM, we ran FVCOM for two cases: one with the same bottom boundary condition as POM and the other with the condition given in (10). Both POM and FVCOM were first run with no mixing and external/internal forcing. Independent of the length of this initial time integration, the water temperature remained unchanged and no velocity was produced. This means that the numerical schemes used in POM and FVCOM don't produce  $\sigma$ -errors in the case with linear distribution of water temperature, no mixing and external/internal forcing.

[56] For a constant background vertical mixing coefficient of  $10^{-4} \text{ m}^2/\text{s}$  and no temperature flux in the vertical direction on the bottom ( $\frac{\partial T}{\partial z} = 0$ ), both POM and FVCOM show that the water temperature near the bottom of the slope

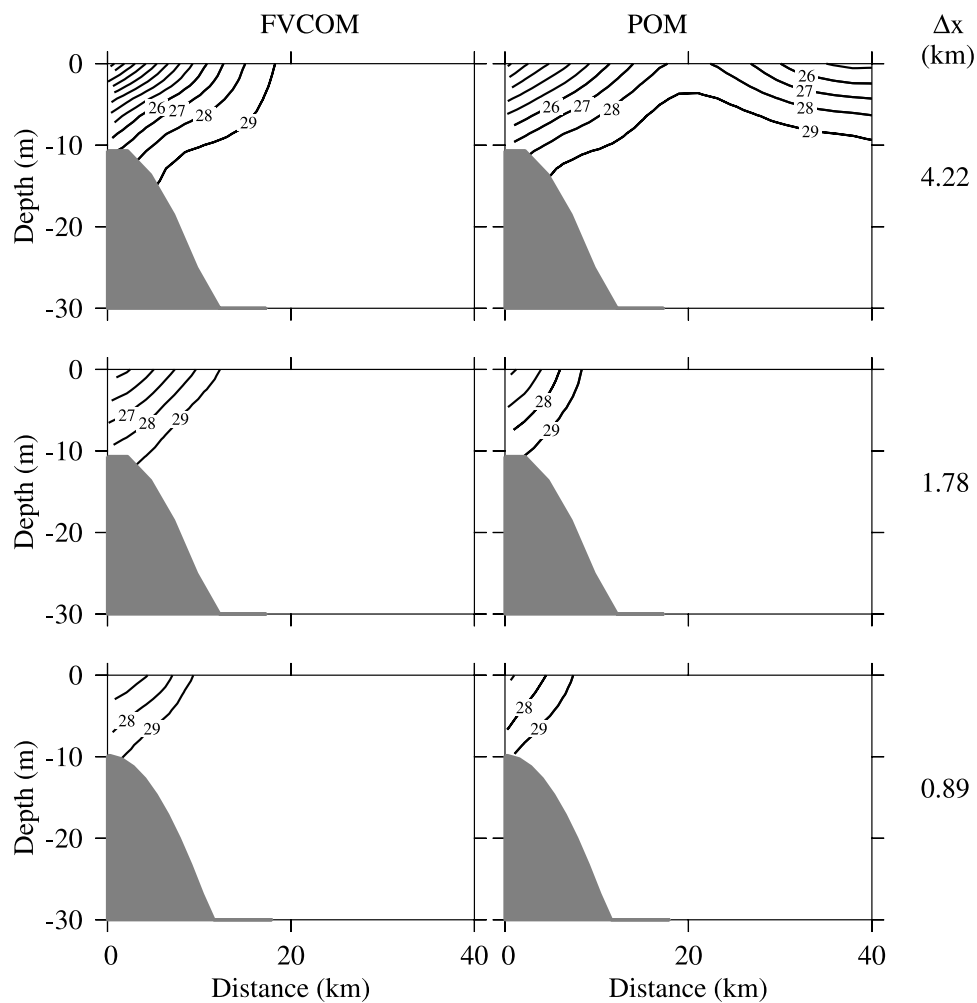


**Figure 21.** Comparison of FVCOM and POM cross-shelf transects at the end of the 10th model from the runs shown in Figure 20.

was mixed to satisfy the bottom boundary condition for temperature. As a result, a thermal boundary layer formed above the bottom due to mixing, and currents arose through momentum adjustments to the resulting horizontal stratification [Wunsch, 1970; Phillips, 1970]. With 31  $\sigma$ -levels in the vertical, the structure of the thermal boundary current predicted by POM and FVCOM depended on the horizontal resolution. For example, with 4.5-km horizontal resolution, both POM and FVCOM developed the multiple layer along-slope boundary currents with time (Figures 26–27). The scale of these currents was the same as the shelf width, and the along-shelf and vertical velocities reached 1 cm/s and  $3 \times 10^{-3}$  cm/s, respectively, after day 10. The pattern of multiple layer currents disappeared in both POM and FVCOM simulations as horizontal grid size decreased to 2.25 km (Figure 28). The currents predicted by these two models were characterized with a two-layer flow: one was near the surface and rotated cyclonically along the coast, and the other was limited to a very thin thermal boundary layer above the bottom of the slope and rotated anticyclonically around the basin. The maximum speed of the along-slope velocity within the thermal boundary layer was about

0.6 cm/s. An upwelling, with a vertical velocity of about  $1 \times 10^{-3}$  cm/s, was found in the thermal boundary layer. These current patterns are consistent with the theory derived by Wunsch [1970]. This theory suggests that a background mixing tends to produce an along-isobath thermal current. Facing downstream in the direction of the current, the lighter water is always on the observer's left. Also, when the pressure gradient forcing moves the water in the interior into the boundary layer, thermal diffusion tends to reduce its density and hence cause it to upwell along the slope.

[57] Our numerical experiments imply that both POM and FVCOM can resolve the structure of the thermal boundary layer over sloping bottom topography at a certain horizontal resolution. The only difference is that FVCOM-predicted currents are symmetrically distributed to the center of the lake, while POM-predicted currents are not. There is no physical reason supporting an asymmetric distribution of the current across the lake for POM, since the numerical grid is composed of squares which are symmetrically distributed around the circular lake and also the mixing coefficient is the same everywhere. The fact that the asymmetric current pattern mainly occurs near the surface

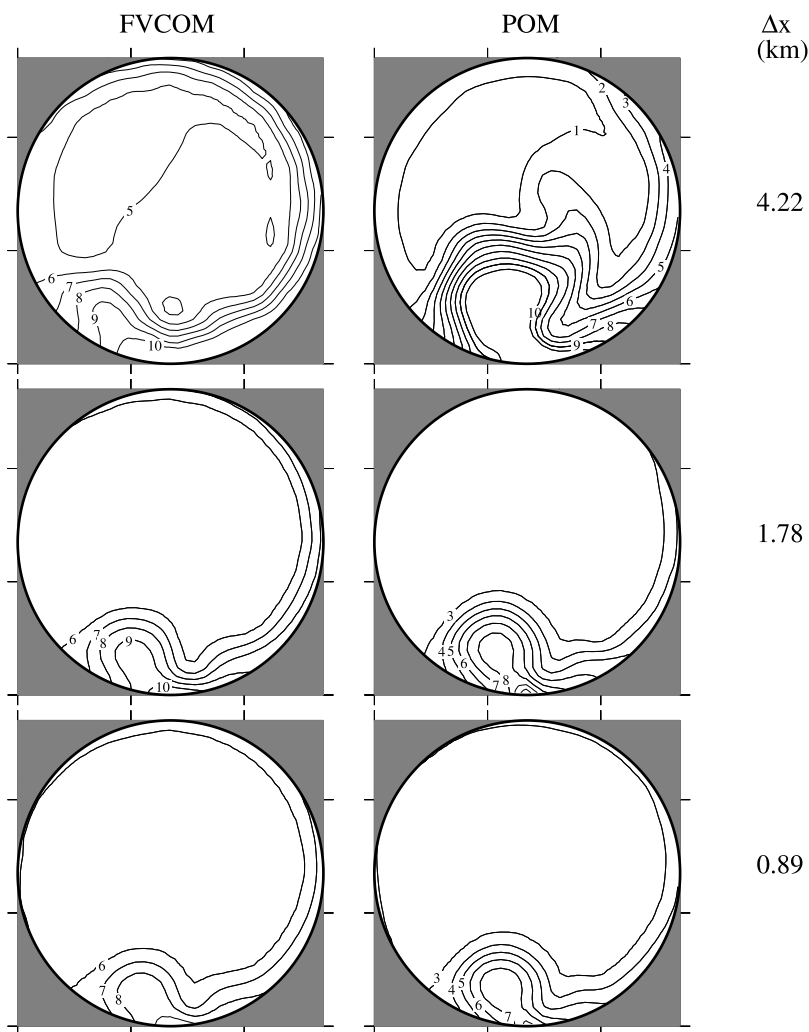


**Figure 22.** Comparison of FVCOM and POM surface elevations at the end of the 10th model day from the runs shown in Figure 20.

around the coast implies that POM has a limitation when applied to a very shallow region. This is probably due to the time-filtering program used in the code and also to the limitation in geometric fitting.

[58] It should be pointed out here that the model results shown above were all based on the bottom boundary condition  $\frac{\partial T}{\partial \sigma} = 0$ . As discussed above, this simplification may lead to an overestimation of vertical mixing and hence horizontal and vertical velocities over a steep slope bottom. Replacing this with the complete bottom boundary condition (10), we reran FVCOM for the case with linear initial stratification and constant background mixing described above. With a given horizontal resolution of 2.25 km, the currents by day 10 predicted by FVCOM were about one order of magnitude weaker than those described above (Figure 29). These results suggest that use of the approximate boundary condition for temperature ( $\frac{\partial T}{\partial \sigma} = 0$ ) can exaggerate vertical mixing and thus overestimates both along-isobath and vertical velocities within the thermal boundary layer that develops over a steeply sloping bottom. This  $\sigma$ -error problem can be minimized in FVCOM by

using the complete condition for no normal heat flux at the boundary (10) over steeply sloping bathymetry.

#### 4. Examples of FVCOM Applications

##### 4.1. Tidal Simulation in the Gulf of Maine/Georges Bank

[59] The Gulf of Maine (GOM)/Georges Bank (GB) region is characterized by near-resonance  $M_2$  tidal motion [Garrett, 1972]. In particular, the  $M_2$  tidal range in the Bay of Fundy (BF) can exceed 8 m, over a factor of 12 greater than the North Atlantic forcing along the shelf break. The nature of tidal resonance in this region is caused by the near-resonance geometry of the entire GOM/GB/BF system rather than a local abrupt change of the bathymetry [Greenberg, 1979]. The GOM/GB/BF is a good region to test FVCOM regarding its capability for simulating tidal waves under a near-resonance condition. There have been many regional modeling efforts made on tidal simulation in this region [e.g., Greenberg, 1979; Lynch and Naimie, 1993; Chen et al., 2001b]. All these models capture the resonance nature of the  $M_2$  tide in the GOM/BF and also provide the

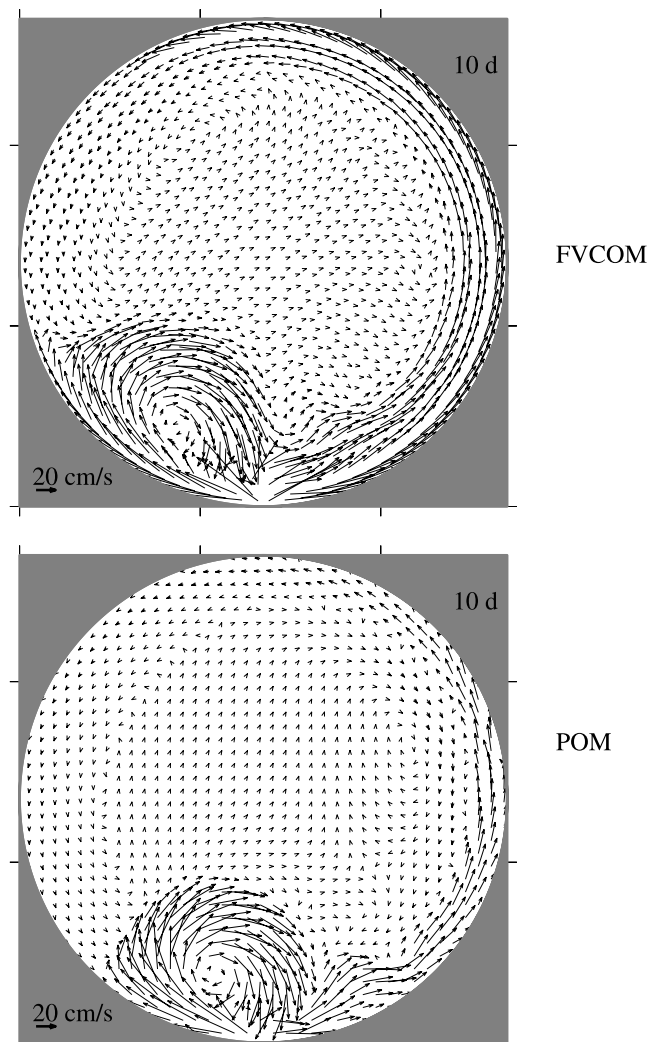


**Figure 23.** Comparison of FVCOM and POM surface current vectors at the end of the 10th model day from the runs shown in Figure 20. The vectors for POM were plotted at every fourth grid point.

reasonable simulation of the amplitudes of tidal elevation in the BF region.

[60] The numerical domain of FVCOM covers the entire GOM/GB/BF region and is enclosed by an open boundary running from the New Jersey shelf to the Nova Scotia shelf (Figure 30, top), with horizontal resolution varying from 1.0 km on the northern flank of GB,  $\sim 2\text{--}3$  km over the southern flank of GB, Browns Bank, and inner shelf coastal regions, and up to 10 km near the open boundary. For comparison with our previous ECOM-si model results [Chen et al., 2001b], we used the same geometric configuration as ECOM-si: the water depth was cut off at 300 m off the shelf break connecting to the open ocean and 31  $\sigma$ -levels with uniform interval were specified in the vertical, which corresponds to a vertical resolution of 3.3 m on the 40-m isobath over GB and adjacent shelf regions and 10 m on the 300-m isobath. Time steps used in FVCOM were 24.84 s for external mode and 248.4 s for internal mode,

which correspond to 180 time steps of the internal mode integration over an  $M_2$  tidal cycle.

[61] FVCOM was forced initially by the barotropic  $M_2$  tidal elevation and phase at the open boundary. These elevations and phases were specified by using values interpolated from results of the Egbert and Erofeeva [2002]  $0.5^\circ \times 0.5^\circ$  inverse tidal model. No open boundary condition for currents was required to be specified in FVCOM, since currents are calculated at the center of each triangular cell, which can be determined through the assumption of mass conservation in the open boundary cell [Chen et al., 2004b].

[62] FVCOM model results were directly compared with the results predicted by ECOM-si. The coverage area of the ECOM-si numerical domain was similar to that of FVCOM's (Figure 30, bottom). All configuration and tidal forcing were the same as those used in FVCOM, except that the ECOM-si grid utilized orthogonal curvilinear coordinates in the horizontal with a horizontal resolution varying from 2.5 to 4 km over GB and in the interior region of the GOM, about 4 km in the cross-bay direction in BF, and 4 to 20 km near the open boundary. To examine the influence of geometric fitting on the nature of the large tidal oscillation in BF, we also ran ECOM-si with 2-km horizontal resolution in the cross-bay direction. In the ECOM-si experiments, a gravity wave radiation condition on current was specified at the open boundary to minimize the reflection of wave energy into the computational domain [Chen and Beardsley, 1995; Chen et al., 2001b]. Time step used in ECOM-si was 414 s for the coarse grid case and 206 s for the finer grid case.

[63] Figure 31 shows the comparison between observed and model-predicted amplitude and phases in the GOM/GB/BF. The data used for the observed chart are composed of  $1/6 \times 1/6$  degree satellite altimeter results and historic tidal measurements. The comparison clearly shows that the FVCOM simulation of the  $M_2$  tidal wave in the GOM/GB/BF is more accurate than ECOM-si. The near-resonance amplitude of the  $M_2$  tidal elevation in BF was captured by FVCOM but not by ECOM-si. The observations show that the maximum amplitude of the  $M_2$  tidal elevation inside the Bay of Fundy exceeds 4 m, which was reproduced by FVCOM but significantly underestimated by ECOM-si. A detailed discussion on tidal simulations done with FVCOM is given in a separate paper (C. Chen et al., Tidal dynamics in the Gulf of Maine and New England Shelf: An application of FVCOM, in revision).

[64] The unstructured grids used in FVCOM provided a better fit with an irregular coastline, which produced a more accurate estimation of the water transport into BF than the structured grid finite difference model ECOM-si. For a given cross-bay horizontal resolution of 4 km, the tidal elevation computed by ECOM-si was about 50 cm lower than that observed in BF. As the horizontal resolution increased, ECOM-si-computed tidal amplitude gradually converged to the observational values but with an increase in phase bias and computing load. With 2-km cross-bay horizontal resolution, the difference in amplitude decreased to  $\sim 10\text{--}25$  cm but the phase bias increased from about  $2^\circ\text{G}$  to over  $10^\circ\text{G}$  (Figure 32).

[65] The comparison results described here are consistent with those found in the Bohai Sea by Chen et al. [2003a],

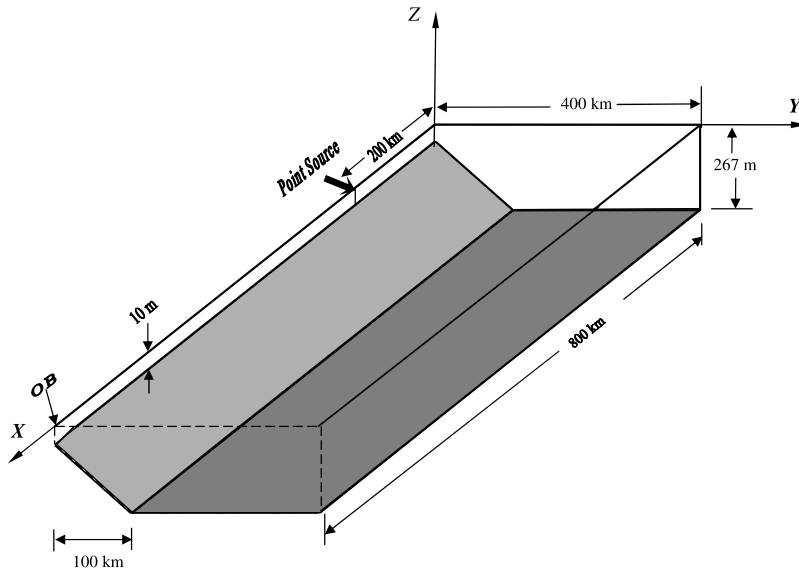


**Figure 24.** Configuration of the idealized, straight coastline continental shelf used for the freshwater discharge case.

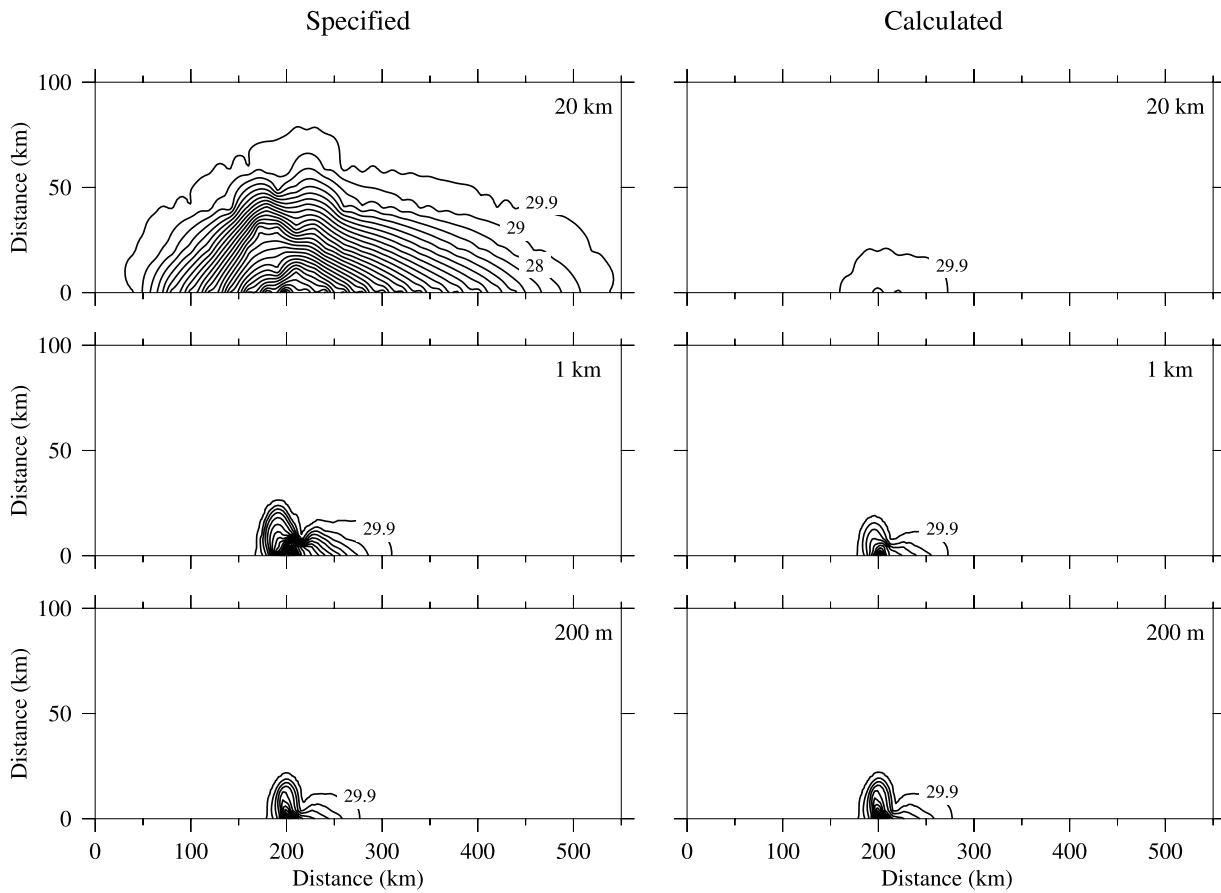


**Figure 25.** Comparison of FVCOM surface salinity at the end of the 5th model day for the cases with “specified” and “calculated” salinity at the node point of the coastal TCE where the freshwater discharge was injected. Horizontal resolution for these experiments was 20 km (top), 1 km (middle), and 200 m (bottom).

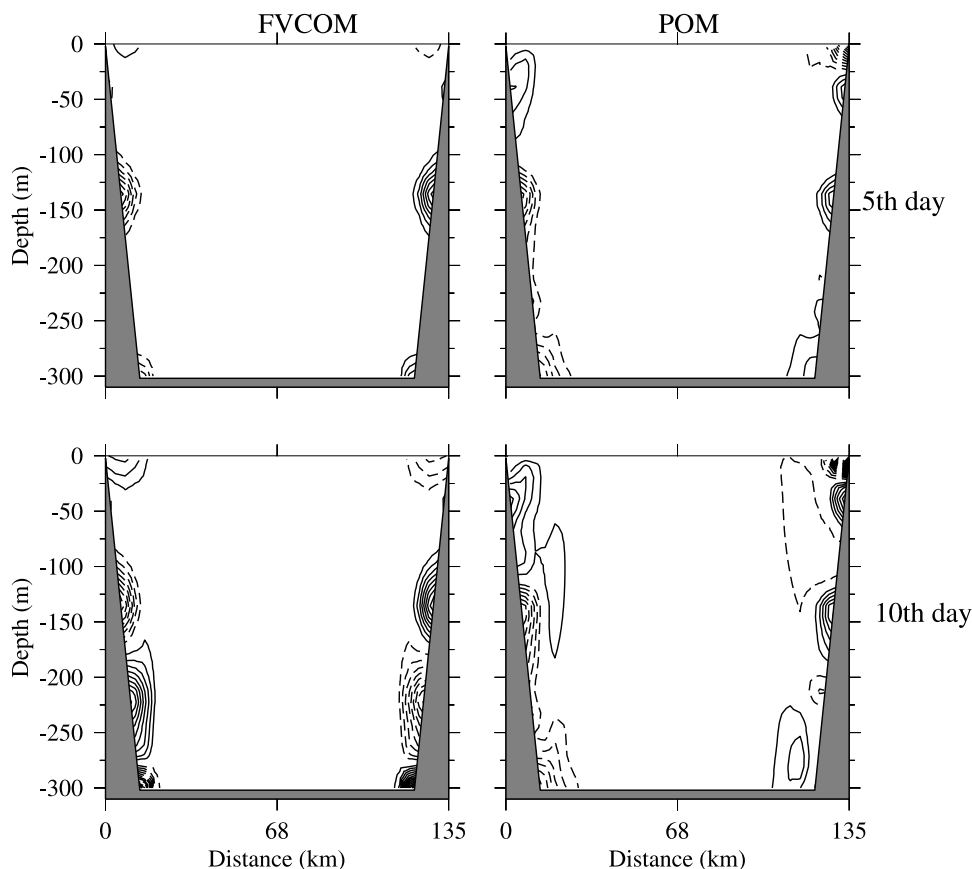


**Figure 26.** Comparison of FVCOM and POM along-shelf currents at the end of the 5th and 10th model days for the idealized circular lake with steep sloping shelf. In this case the initial water temperature profile was linear in the vertical. No external and internal forcings were applied. The background mixing was set to  $10^{-4} \text{ m}^2/\text{s}$ . Horizontal resolution for both FVCOM and POM was 4.5 km. Contour interval is 0.1 cm/s.

who pointed out that FVCOM reproduced the near-resonance amplitude and phase of tidal elevation in the Bohai Sea but ECOM-si failed. These realistic applications support our finding for the idealized cases described in section 3.2, which show that the mismatch in coastal geometry fitting can produce a big bias in the phase of the tidal wave in near-resonance conditions.

[66] We also checked the tidal simulation results from QUODDY (an unstructured grid finite element model developed at Dartmouth College by D. Lynch and co-workers that has been used for the Gulf of Maine in the last 10 years). While we think that QUODDY should also reproduce the amplitudes and phases of the  $M_2$  tide in the GOM/GB/BF system., past studies with QUODDY published by Lynch and Naimie [1993] did not include the upper BF region, so no model-model-data comparisons were made at stations in that region where the  $M_2$  elevation exceeds 3 m.

[67] Recently, Dupont et al. [2005] applied a 2-D finite element model (MOG-2D) to simulate the tidal motion in the upper region of BF. The MOG-2D is an unstructured grid model developed by Carrère and Lyard [2003]. By resolving accurately the complex geometry with a horizontal resolution of 0.03–5.0 km, this unstructured grid model reproduced the large dominant  $M_2$  tidal elevation within an RMS error of 10% relative to the observation. Their studies

support a need for an unstructured grid model to resolve the resonant tidal structure in BF.

#### 4.2. Tidal-Rectified Currents on Georges Bank

[68] Observations have revealed that the nonlinear interaction of tidal currents over the abrupt bottom topography of GB generates a clockwise residual current on GB [Butman et al., 1982; Limeburner and Beardsley, 1996]. This current tends to flow eastward as a jet of  $\sim 30 \text{ cm/s}$  on the northern flank and recirculate westward as a relatively weak, broad current of about 1–5 cm/s on the southern flank. Previous theoretical and numerical modeling studies suggest that the strong current jet formed on the northern flank is a result of (1) nonlinear interaction of barotropic tidal current with variable bottom topography [Loder, 1980; Greenberg, 1983], (2) seasonal stratification due to surface heating and intensification of the tidal mixing front [Chen, 1992; Naimie et al. 1994; Chen et al., 1995, 2001b; Naimie, 1996], (3) nonlinear interaction between barotropic and internal tidal currents and between internal tidal currents [Chen and Beardsley, 1995, 1998], and (4) upstream buoyancy-driven flow [Chapman and Beardsley, 1989; Chapman, 2003].

[69] For the same given  $M_2$  tidal forcing, both FVCOM and ECOM-si predicted a clockwise residual circulation

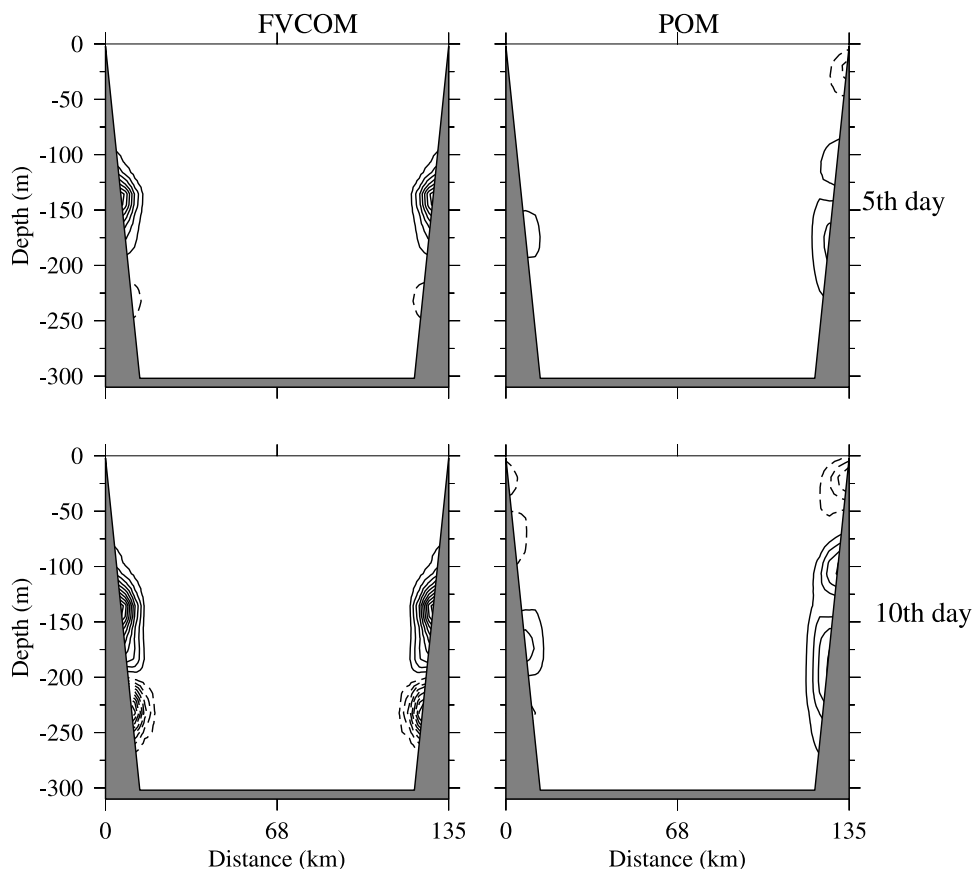


**Figure 27.** Comparison of FVCOM and POM vertical velocities at the end of the 5th and 10th model days from the runs shown in Figure 29. Contour interval is  $0.4 \times 10^{-3}$  cm/s.

over GB (Figure 33). FVCOM showed a strong current jet of about 20–25 cm/s flowing along the local isobaths on the northern flank and the weakly return flow of 5–8 cm/s over the southern flank of GB, generally consistent with observation [Butman *et al.*, 1982] and very similar to that predicted by QUODDY [Lynch and Naimie, 1993; Naimie *et al.*, 1994]. ECOM-si with a horizontal resolution of about 2.5–4 km over GB showed a significant bias in the direction of the residual current on the bank, which resulted in an overestimation of the cross-isobath water transport. As the horizontal resolution in ECOM-si increased, the residual pattern predicted by ECOM-si gradually converged to the pattern predicted by FVCOM. This is consistent with our assumption that all the primitive equation coastal ocean circulation models should converge toward the same numerical solution since they solve the same governing equations. However, the speed of the convergence may differ significantly because of the different numerical methods used in each model. For applications to regions with complex geometry such as the GOM/GB/BF, the flexible unstructured grid approach used in FVCOM provides faster convergence and higher numerical efficiency than the finite difference models considered.

#### 4.3. Impact of the Bottom Boundary Condition on the Stratified Residual Current

[70] The idealized circular lake experiment in section 3.4 suggests that use of the simplified bottom boundary condi-

tion  $\frac{\partial T}{\partial \sigma} = 0$  over a sloping bottom can lead to an overestimate of vertical mixing and thus the buoyancy-driven thermal boundary current over the slope. Since the bottom boundary condition of no temperature flux in the vertical has been widely used in coastal ocean models, it is valuable to provide a quantitative estimation of the numerical errors caused by this simplification for a realistic coastal ocean domain. For this we consider GB which has steep flanks and strong tidal mixing over its top. The temperature and salinity fields on GB feature a tidal mixing front located around 40-m (northern flank) and 60-m (southern flank) isobaths and a density front at the shelf break starting at the bottom near the 100-m isobath. Using the monthly climatological temperature and salinity fields to initialize FVCOM and  $M_2$  tidal forcing along the open boundary, we ran two simulations, the first with no flux of temperature and salinity in the vertical and the second with no flux of temperature and salinity normal to the slope of the bottom topography (10). In both cases, the horizontal diffusion  $A_m$  was estimated using the Smagorinsky eddy parameterization method.

[71] The comparison shows that the simplified bottom boundary condition overestimated vertical mixing over the sloping bottom topography of the bank (Figure 34). On the southern flank, the thickness of the bottom mixed layer was increased to about 10–20 m and the contours of temperature shifted offbank by about 10 km. At the shelf break, the height of the bottom mixed layer also increased about 10–

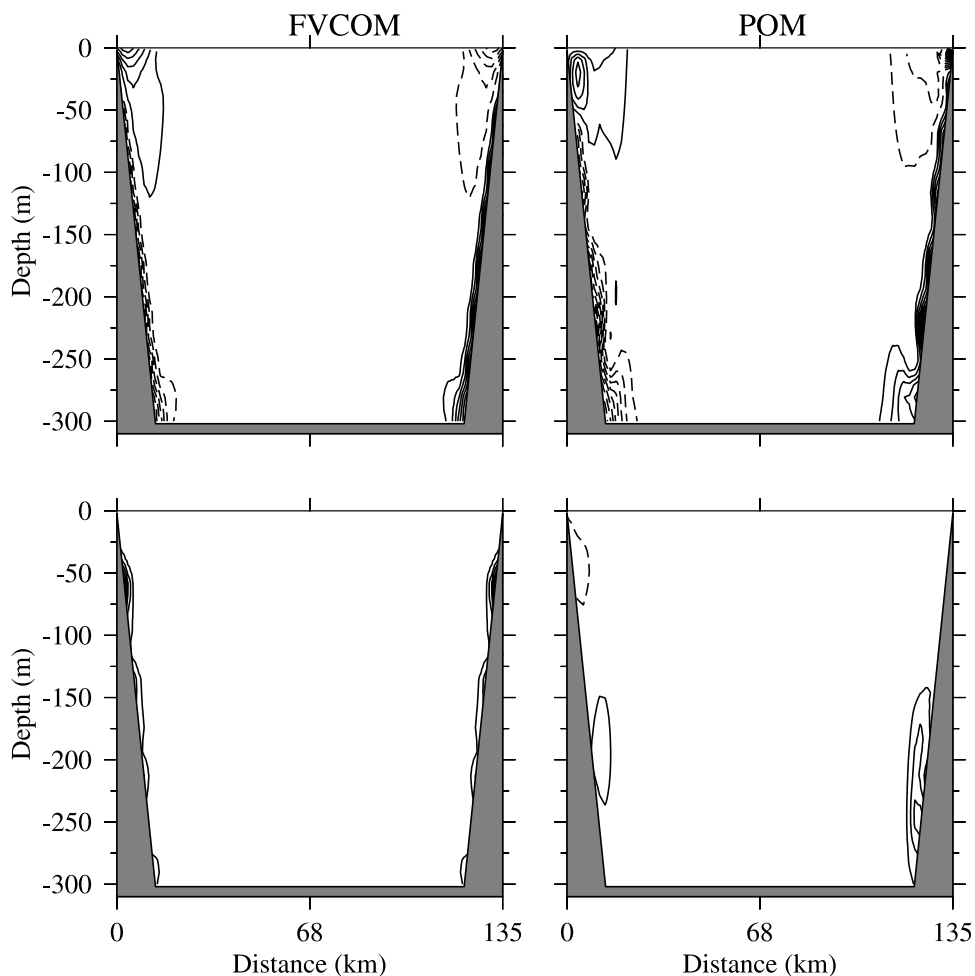


**Figure 28.** Comparison of FVCOM and POM along-shelf and vertical velocities at the end of the 10th model day between FVCOM and POM from the runs with 2.25-km horizontal resolution. Contour interval is 0.1 cm/s for  $u$  and  $0.4 \times 10^{-3}$  cm/s for  $w$ .

20 m. The  $10^{\circ}\text{C}$  contour shifted downward, about 20 m in the vertical and 2 km in the horizontal. Similar results were also evident in the salinity field. As a result, the spatial structure of the along-bank stratified residual current shifted offbank, with an increase of about 2–3 cm/s in magnitude. The numerical experiments conducted in section 3.4 show that the simplified bottom temperature condition will increase the magnitude of upwelling in the thermal boundary layer over the slope. This is also indirectly evident in the current case, where the downwelling velocity near the bottom of the slope was weaker in the case with the simplified bottom condition of temperature and salinity than in the case with the complete bottom condition described in (10) and (14). The change of vertical velocity near the bottom slope for these two cases was about 1 cm/s.

[72] Our experiments indicate that the error in velocity caused by the simplified bottom boundary conditions for temperature and salinity depends on both the horizontal and vertical resolution used in the model. This can be easily understood because assuming no flux in the vertical results in an overestimation of vertical mixing, and hence enlarges the horizontal density gradients and the vertical scale of the sloping bottom boundary layer. Since numerical errors of

vertical gradients of temperature and salinity increase with a decrease in horizontal and vertical resolution, it is without a doubt that the impact of incorrect bottom boundary conditions of temperature and salinity on numerical solutions become more significant as numerical resolution decreases. These errors might be much bigger than the  $\sigma$ -coordinate error over steep topography (e.g., near the shelf break). Therefore they definitely cannot be ignored in model applications to the shelf break, banks, and other regions characterized by steep bottom topography.

## 5. Discussion and Conclusion

[73] Comparisons between FVCOM, POM and ECOM-si solutions for a variety of test cases with idealized and realistic bathymetry demonstrate that the finite volume method used in FVCOM provides a more accurate simulation than the two finite difference models in cases with complex coastal geometry and steep bottom slopes. In particular, the finite volume method ensures volume, mass, and tracer conservation in the individual control volumes and the unstructured triangular grid can be closely fit to irregular coastlines and model domains, resulting in highly

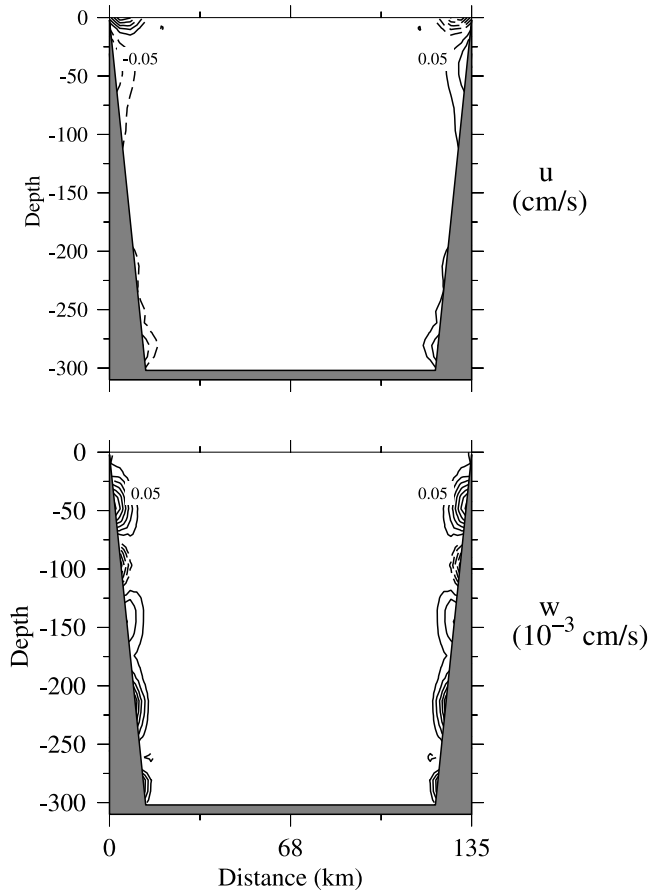


**Figure 29.** FVCOM along-shelf and vertical velocities at the end of the 10th model day for the case with the exact bottom boundary condition of no temperature flux into the bottom (10). Contour interval is 0.05 cm/s for  $u$  and  $0.05 \times 10^{-3}$  cm/s for  $w$ .

accurate numerical solutions in even quite complex model geometries. With second-order accuracy, FVCOM combines the advantage of a finite element method for geometric flexibility and a finite difference method for simple discrete computation.

[74] The importance of geometric fitting on the accuracy of numerical simulation has been examined in many previous model validation experiments for both unstructured and structured grid cases [e.g., *Haidvogel and Beckmann, 1999; Dupont et al., 2003*]. For the western boundary layer test case, *Haidvogel and Beckmann [1999]* found that the unstructured grid spectral finite element method showed faster convergence than structured grid finite difference methods. *Dupont et al. [2003]* pointed out from their studies on the impact of a step-like coastline on the basin-scale vorticity budget of the subtropic gyre that the rectangular grid-induced step-like lateral boundary may have direct impact of the accuracy of the vorticity calculation of the gyre and that this error could not be easily suppressed by increasing the horizontal resolution. These results support the numerical model results presented in this text.

[75] POM and ECOM-si have been widely used in ocean science in the last 20 years. In particular, these two models have been successfully applied in regional and coastal ocean

studies to investigate and understand key physical processes. The idealized model comparisons presented here and elsewhere emphasize the importance of coastline fitting and numerical methods when simulating flows in complex coastal and estuarine domains. On the basis of our experience with these two finite difference models and FVCOM, we believe that the future of coastal/estuarine modeling should move toward unstructured grid models that provide excellent geometric matching and improved numerical schemes.

[76] Because of the current limitation in computational capability, coastal modeling efforts are usually focused on a specific coastal region surrounded by an open boundary. This approach makes it easy to examine the response of the coastal ocean to local forcing, but causes both limitations in the ocean processes that can be included and numerical difficulties in dealing with open boundary conditions. As computer power increases, it will become feasible and desirable to extend the global ocean model to cover the coastal regions in more detail. The geometric flexibility inherent in an unstructured grid model could provide a better alternative to bridge the global and coastal ocean models.

#### Appendix A: Temperature or Salinity Boundary Condition Over a Sloping Bottom

[77] Considering bottom topography with a slope  $\alpha$  in the coordinate system shown in Figure A1 where  $n$  is the direction of the horizontal gradient of the slope, the bottom boundary condition of no heat (temperature) flux into the slope can be written as

$$K_h \frac{\partial T}{\partial z} - A_H \frac{\partial T}{\partial n} \tan \alpha = 0 \quad (\text{A1})$$

where  $K_h$  and  $A_H$  are the vertical and horizontal diffusivities, respectively. This condition was first introduced in the study of upwelling over bottom topography by *Pedlosky [1974]* and suggested to be incorporated into FVCOM by Dave Chapman (personal communication) at the Woods Hole Oceanographic Institution.

[78] Rewriting (A1) in the  $\sigma$ -coordinate transformation coordinate system yields

$$\frac{K_h}{D} \frac{\partial T}{\partial \sigma} - A_H \left( \frac{\partial T}{\partial n} + \frac{\partial T}{\partial \sigma} \frac{\partial \sigma}{\partial n} \right) \tan \alpha = 0 \quad (\text{A2})$$

or

$$\left( \frac{K_h}{D} - A_H \frac{\partial \sigma}{\partial n} \tan \alpha \right) \frac{\partial T}{\partial \sigma} = A_H \frac{\partial T}{\partial n} \tan \alpha. \quad (\text{A3})$$

Because

$$\frac{\partial \sigma}{\partial n} = -\frac{1}{D} \left[ (1 + \sigma) \frac{\partial \zeta}{\partial n} + \sigma \frac{\partial H}{\partial n} \right] = -\frac{1}{D} \left[ (1 + \sigma) \frac{\partial \zeta}{\partial n} - \sigma \tan \alpha \right], \quad (\text{A4})$$

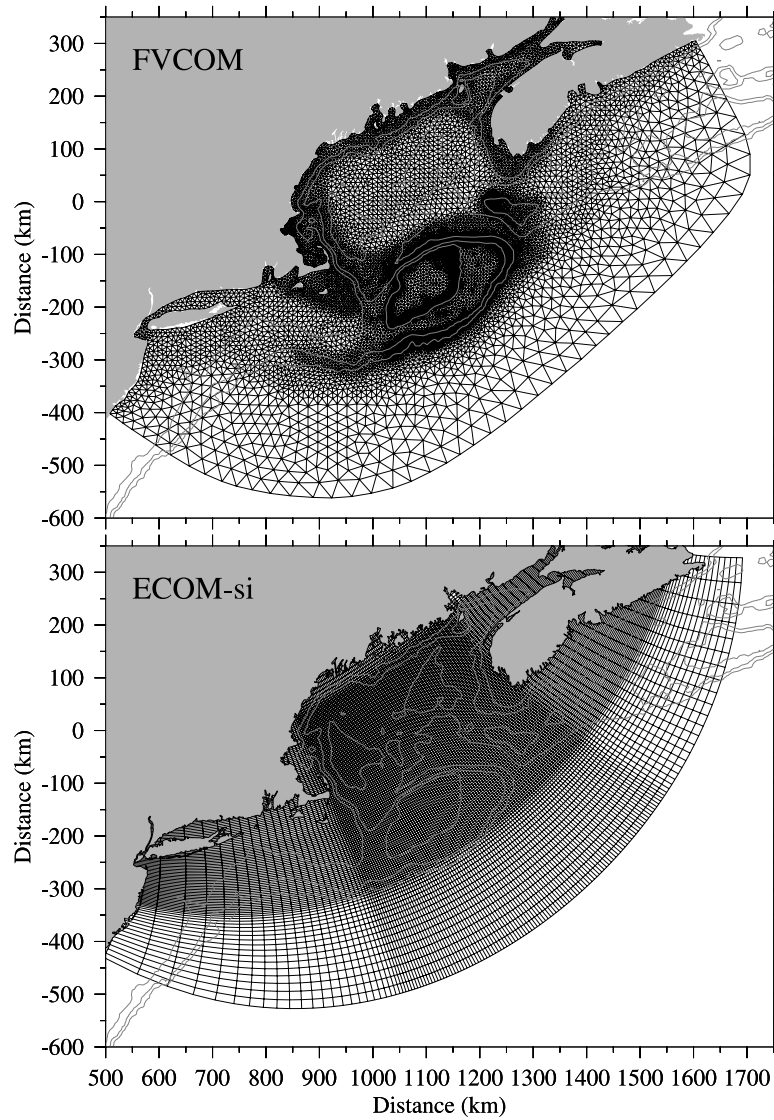


**Figure 30.** Numerical grids used for FVCOM (top) and ECOM-si (bottom). The horizontal resolution for FVCOM is 1–2 km on the northern flank of Georges Bank and 3–4 km on the top of the bank and 10–20 km off the shelf near the open boundary. The horizontal resolution for ECOM-si is 2–3 km on Georges Bank and 10 km off the shelf near the open boundary.

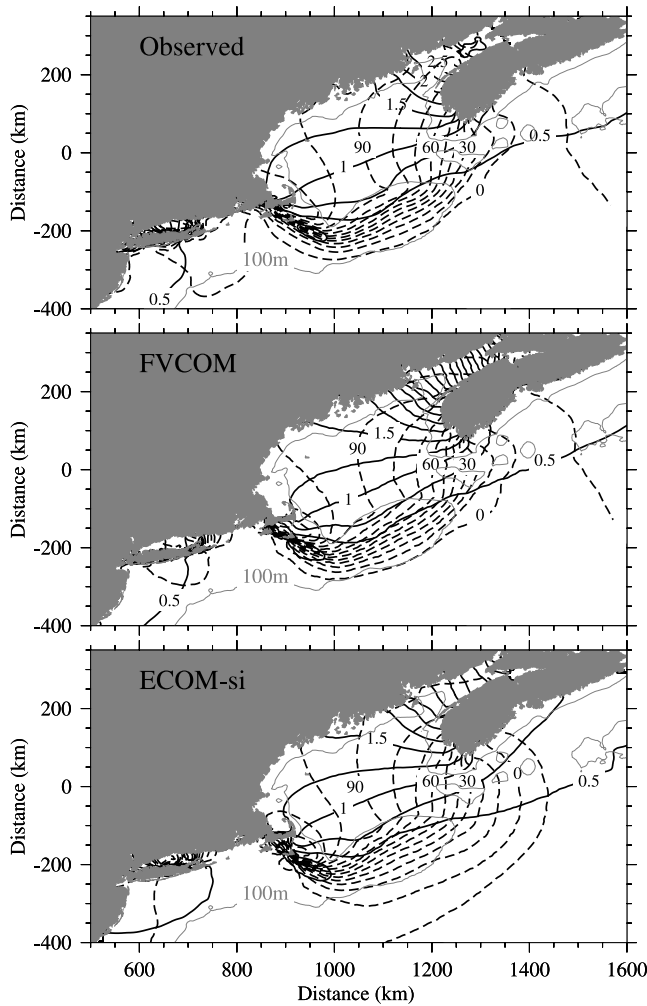


**Figure 31.** Comparison between observed (top) and model-predicted (middle and bottom)  $M_2$  tidal amplitudes and phases in the Gulf of Maine/Georges Bank region. Figure 31, middle: FVCOM, and bottom: ECOM-si.

and  $\sigma = -1$  at the bottom, (A3) can be rewritten as

$$\left\{ \frac{K_h}{D} + \frac{A_H}{D} \tan^2 \alpha \right\} \frac{\partial T}{\partial \sigma} = A_H \frac{\partial T}{\partial n} \tan \alpha. \quad (\text{A5})$$

Therefore the boundary condition for temperature on a sloping bottom is

$$\frac{\partial T}{\partial \sigma} = \frac{A_H D \tan \alpha}{K_h + A_H \tan^2 \alpha} \frac{\partial T}{\partial n}. \quad (\text{A6})$$

[79] Replacing  $T$  by  $S$  in (A6), we derive the bottom boundary condition for salinity as

$$\frac{\partial S}{\partial \sigma} = \frac{A_H D \tan \alpha}{K_h + A_H \tan^2 \alpha} \frac{\partial S}{\partial n}. \quad (\text{A7})$$

[80] To determine the vertical gradient of temperature or salinity at the bottom in (A6) or (A7), we need to calculate accurately the bottom slope  $\alpha$  and the horizontal gradient of temperature or salinity perpendicular to the bottom  $\partial T/\partial n$  or  $\partial S/\partial n$ . In FVCOM,  $\alpha$  and  $\partial T/\partial n$  or  $\partial S/\partial n$  are calculated using a simple Green's theorem by which the area integration can be solved by the trajectory integration of the boundary of the area.

## Appendix B: Methods to Add the Discharge From the Coast or a River

[81] FVCOM incorporates two methods to include the freshwater discharge or tracer transport from the coastal solid boundary. One is to inject the water into the tracer control element (TCE) (Figure B1) and the other is to input the water into the momentum control element (MCE) (Figure B2). In each method, the tracer concentration (such as salinity, temperature or others) can be either specified or calculated through the tracer equation. The discrete expressions for these two approaches are described in detail below.

### B1. The TCE Method

[82] Define that  $Q$  is the water volume transport into a TCE with an area of  $\Omega^s$  and a depth of  $D$  (shown in Figure B1). The surface elevation at the coastal node in this TCE can be calculated by

$$\frac{\partial \zeta}{\partial t} = \left[ - \oint_s v_n D ds + Q \right] / \Omega^s, \quad (\text{B1})$$

where  $v_n$  is the velocity component normal to the boundary line of the TCE and  $s$  is the closed trajectory of the boundary of the TCE.

[83] The way to include  $Q$  in the continuity equation is equivalent to adding the flux into a TCE from its coastal boundary lines (see the heavy line shown in Figure B1). Since this boundary line links to two momentum control elements (MCE), the contribution of  $Q$  to the momentum in these two elements needs to be taken into account.

[84] For the external model, defining that  $l_i$  and  $l_j$  are half a length of the coastal sideline of triangles with areas of  $\Omega_i$  and  $\Omega_j$ , respectively, the vertically averaged  $x$  and  $y$  components of the velocity resulting from  $Q$  are equal to

$$U_o = \frac{Q \cos \hat{\theta}}{D(l_i + l_j)}, V_o = \frac{Q \sin \hat{\theta}}{D(l_i + l_j)} \quad (\text{B2})$$

where  $\hat{\theta}$  is the angle of the coastline relative to the  $x$  direction. The contributions of  $Q$  to the  $x$  and  $y$  vertically integrated momentum equations in the MCE with an area of  $\Omega_i$  or  $\Omega_j$  are given as  $0.5QU_o$  and  $0.5QV_o$ , respectively.

[85] For the internal mode, let  $R_{Qk}$  be the percentage of  $Q$  in the  $k$ th sigma layer which satisfies the condition of

$$\sum_{k=1}^{KM-1} R_{Qk} = 1, \quad (\text{B3})$$

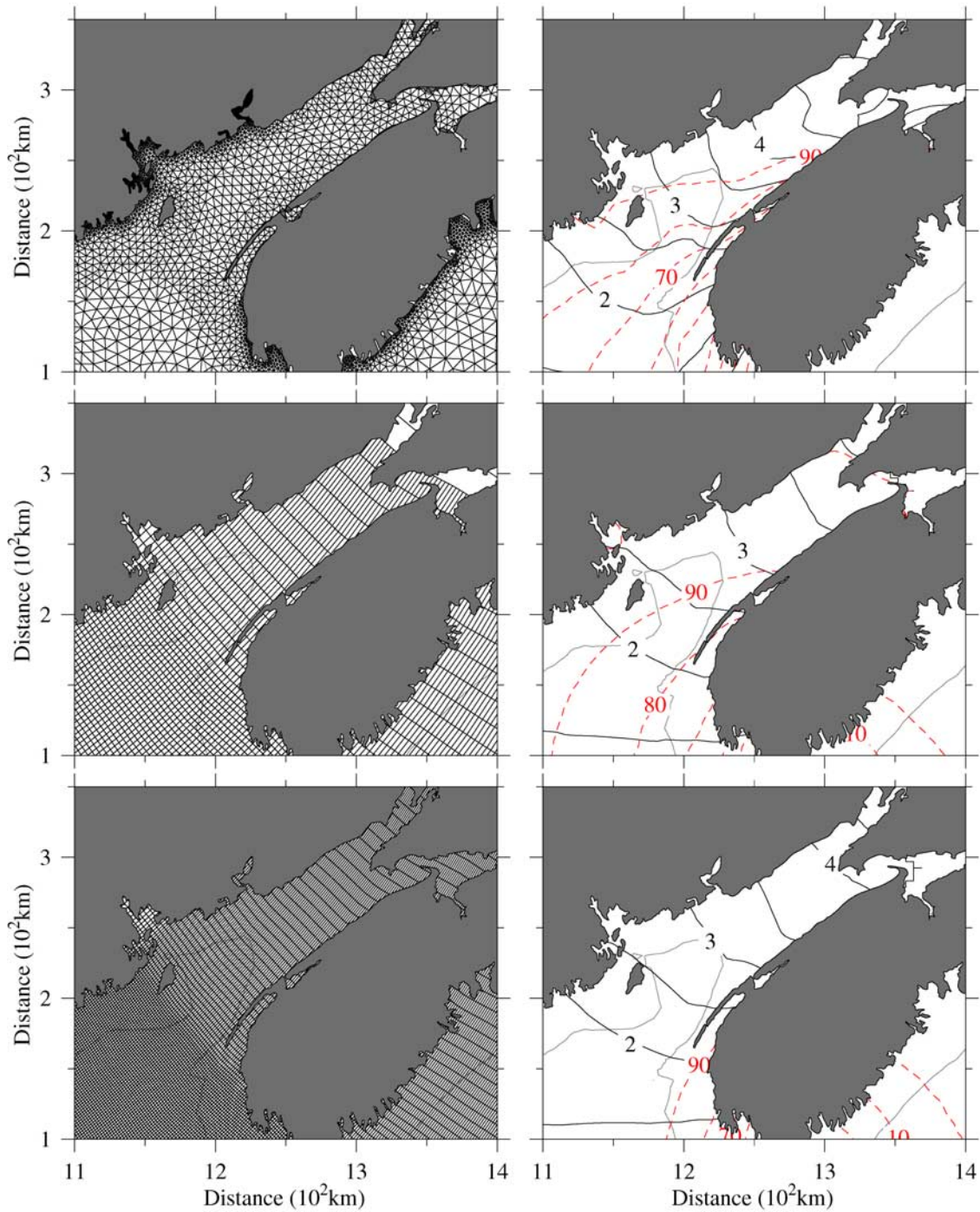


**Figure 32.** Model-computed distributions of the  $M_2$  tidal amplitude and phase in the Bay of Fundy (BF) for FVCOM and ECOM-si. The horizontal resolution of FVCOM in BF ranges from 0.5 km inside inlets to 2 km along the coast and 4 km in the interior of the bay. ECOM-si grid sizes are about 4 km in the cross-bay direction and 8–10 km in the along-bay direction for the coarse resolution case (middle) and about 2 km in the cross bay direction and 4–5 km in the along-bay direction for the finer resolution case (bottom).

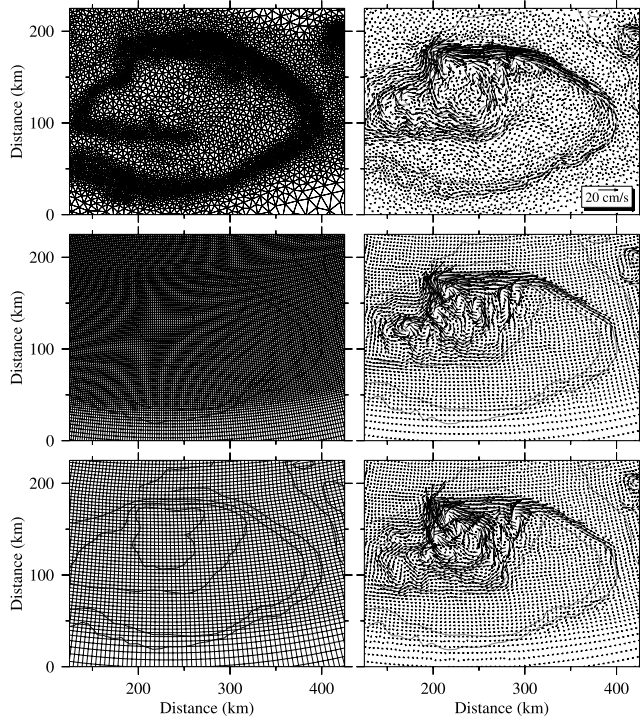


**Figure 33.**  $M_2$  tidal residual current vectors over Georges Bank and adjacent regions for FVCOM (top) and ECOM-si (middle and bottom).

where  $KM$  is the number of sigma levels in the vertical. The transport entering the  $k$ th sigma layer in the TCE is equal to  $QR_{Qk}$  and the  $x$  and  $y$  components of the velocity resulting from this amount of water transport are given as

$$U_{ok} = \frac{QR_{Qk} \cos \hat{\theta}}{D(l_i + l_j) \Delta \sigma_k}; V_{ok} = \frac{QR_{Qk} \sin \hat{\theta}}{D(l_i + l_j) \Delta \sigma_k} \quad (B4)$$

where  $\Delta \sigma_k$  is the thickness of the  $k$ th sigma layer. Therefore the contribution of  $QR_{Qk}$  to the  $x$  and  $y$  momentum equation in the  $k$ th sigma layer of the MCE with an area of  $\Omega_i$  or  $\Omega_j$  are given as  $0.5QR_{Qk}U_{ok}$  and  $0.5QR_{Qk}V_{ok}$ , respectively.

[86] The tracer concentration (such as salinity, temperature, or others) at the coastal node of the TCE can be either specified or calculated. For the first case, the tracer concentration at the coastal node is specified by users at each time step, so that no calculation is needed to solve the tracer equation for the TCE where  $Q$  is added. This method is built on an assumption that no mixing occurs in the TCE where the water is injected from the coast or a river. It is also the method that is usually used in finite difference models in studies of point source buoyancy-forced flow. The advantage of this method is simplicity, however, it might cause unrealistic buoyancy gradients near the discharge source, especially in models with coarse horizontal resolution.

[87] For the second case, the tracer concentration at the coastal node where  $Q$  is added is calculated directly from the tracer equation, with an assumption that the water injected into the system directly contributes to the tracer transport in the TCE (where the discharge source is located) and the tracer concentration at the coastal node of this TCE

is determined by the adjusted net tracer flux and mixing. For example, defining  $S_{ok}$  as the salinity in the  $k$ th sigma layer at the coastal node of the TCE where  $Q$  is added, the salinity equation in integral form reduces to

$$\frac{\partial S_{ok} D}{\partial t} = \left[ - \oint_{s-(l_i+l_j)} v_{nk} S_k D ds + \iint_{\Omega^c} F_s dx dy + QR_{Qk} \hat{S}_{ok} \right] / \Omega^c \quad (B5)$$

where  $v_{nk}$  is the velocity component normal to the boundary line of the TCE in the  $k$ th sigma layer,  $S_k$  is the salinity at nodes of triangles connecting to the coastal node of the TCE,  $F_s$  is the horizontal and vertical diffusion terms in the salinity equation, and  $\hat{S}_{ok}$  is the salinity contained in the water volume of  $Q$ .

## B2. The MCE Method

[88] Let  $Q$  be the water volume transport into a MCE,  $\hat{\theta}$  the angle of the coastline relative to the  $x$  direction, and  $l$  the

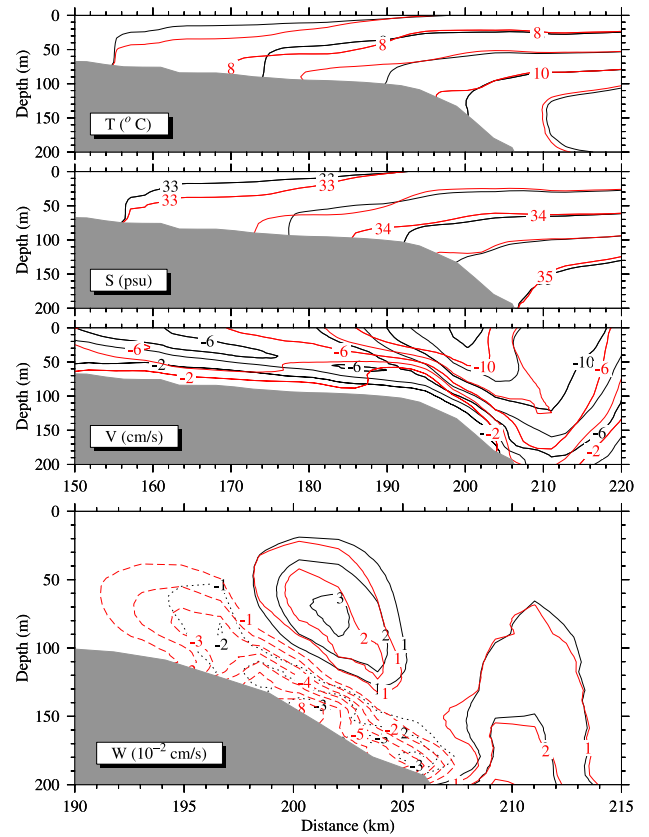


**Figure 34.** Comparison of model-predicted cross-shelf tidally averaged temperature, salinity, along-bank current and vertical velocity for runs with simplified (black) and exact (red) bottom boundary conditions of temperature and salinity. The initial fields of temperature and salinity were specified using January climatologically averaged hydrographic data. The model was driven by the  $M_2$  tidal forcing only.

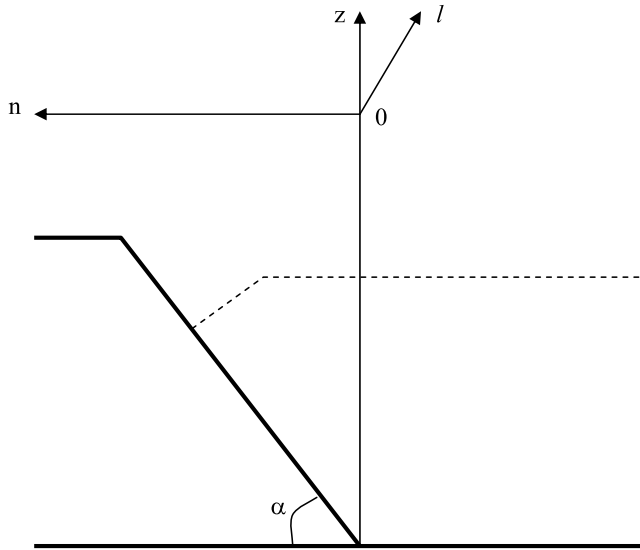


**Figure A1.** Schematic of sloping bottom geometry.

length of the coastal boundary of the MCE (Figure B2). The vertically averaged  $x$  and  $y$  components of the velocity driven by  $Q$  can be estimated as

$$U_o = \frac{Q}{Dl} \cos \hat{\theta}; V_o = \frac{Q}{Dl} \sin \hat{\theta}. \quad (\text{B6})$$

Using the same definition of  $R_{Qk}$  described in B.3, the  $x$  and  $y$  components of the velocity in the  $k$ th sigma layer in the MCE are given as

$$U_{ok} = \frac{QR_{Qk} \cos \hat{\theta}}{Dl \Delta \sigma_k}; V_{ok} = \frac{QR_{Qk} \sin \hat{\theta}}{Dl \Delta \sigma_k}. \quad (\text{B7})$$

Therefore the contributions of the freshwater discharge to the external  $x$  and  $y$  momentum equations of the MCE are

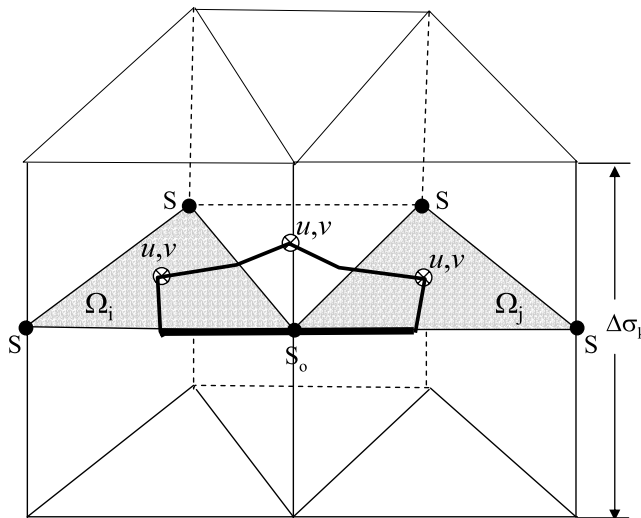


**Figure B1.** Grid configuration for freshwater discharge at a node point of a TCE.

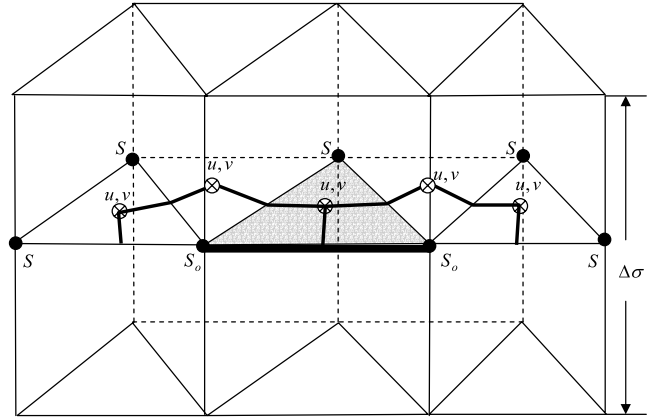


**Figure B2.** Grid configuration for freshwater discharge at a boundary line of a MCE.

$QU_o$  and  $QV_o$ , respectively, while the contributions to the internal  $x$  and  $y$  momentum equations of the MCE in the  $k$ th sigma layer are equal to  $QR_{Qk}U_{ok}$  and  $QR_{Qk}V_{ok}$ , respectively.

[89] Because the freshwater discharge is injected in the computational domain from a single MCE, we assume that there is an along-coastal gradient of sea level built due to this discharge. A simple way to satisfy this condition is to choose the same geometric shape for two surrounding TCEs that connected to the MCE where the freshwater input and assume that the freshwater flows equally into these two TCEs. Let  $i$  and  $j$  represent the two TCEs connected to the freshwater source, then

$$Q_i = Q_j = Q/2. \quad (\text{B8})$$

Note that this assumption is only valid when the two surrounding TCEs have the same geometric shapes. Therefore the surface elevation at the coastal node in  $i$ th and  $j$ th TCEs can be calculated by

$$\frac{\partial \zeta_I}{\partial t} = \left[ - \oint_s v_{nI} D_I ds + Q_I \right] / \Omega_I^\zeta, \quad (\text{B9})$$

where  $I$  are either  $i$  or  $j$ , and  $v_{nI}$  is the velocity component normal to the boundary line of the  $I$ th TCE and  $s$  is the closed trajectory of the boundary of this TCE.

[90] The tracer concentration (such as salinity, temperature, or others) at the coastal node of the  $i$ th or  $j$ th TCE also can also be either specified or calculated. The method used to include the freshwater discharge into the tracer equation is the same as that described above in the TCE method.

[91] **Acknowledgments.** This research was supported by the U.S. GLOBEC Northwest Atlantic/Georges Bank program through NSF grants OCE-0234545, OCE-0227679, NOAA grant NA 160P2323, and NSF CoOP grant OCE-0196543 to C. Chen and NSF OCE-0227679 and the WHOI Smith Chair to R. C. Beardsley, H. Huang and Q. Xu were supported by Chen's Georgia and South Carolina Sea Grant awards NA06RG0029 and NA960P0113. G. Cowles was supported by the SMAST fishery program through NOAA grants DOC/NOAA/NA04NMF4720332 and DOC/NOAA/NA05NMF4721131. Lixia Wang, former research associate at SMAST/UMASSD, assisted H. Liu in conducting POM and ECOM-si experiments for wind-driven oscillation and the bottom thermal

boundary layer cases in the early status of this study. Her contributions are acknowledged here. This paper is U.S. GLOBEC contribution number 294 and 06-0501 in the SMAST Contribution Series, School of Marine Science and Technology, University of Massachusetts-Dartmouth.

## References

- Birchfield, G. E. (1969), Response of a circular model great lake to a suddenly imposed wind stress, *J. Geophys. Res.*, *74*, 5547–5554.
- Birchfield, G. E., and B. P. Hickie (1977), The time-dependent response of a circular basin of variable depth to a wind stress, *J. Phys. Oceanogr.*, *7*, 691–701.
- Blumberg, A. F. (1994), A primer for ECOM-si, technical report, 66 pp., HydroQual, Mahwah, N. J.
- Blumberg, A. F. and G. L. Mellor (1987), A description of a three-dimensional coastal ocean circulation model, in *Three-Dimensional Coastal Models, Coastal Estuarine Ser.*, vol. 3, edited by N. S. Heaps, pp. 1–16, AGU, Washington, D. C.
- Butman, B., R. C. Beardsley, B. Magnell, D. Frye, J. A. Vermersch, R. Schlitz, R. Limeburner, W. R. Wright, and M. A. Noble (1982), Recent observations of the mean circulation on Georges Bank, *J. Phys. Oceanogr.*, *12*, 569–591.
- Carrère, L., and F. Lyard (2003), Modeling the barotropic response of the global ocean to atmospheric wind and pressure forcing: Comparisons with observations, *Geophys. Res. Lett.*, *30*(6), 1275, doi:10.1029/2002GL016473.
- Casulli, V. (1990), Semi-implicit finite difference methods for the two-dimensional shallow water equations, *J. Comput. Phys.*, *86*, 56–74.
- Chao, S. Y. (1988), Wind-driven motion of estuarine plumes, *J. Phys. Oceanogr.*, *18*, 1144–1166.
- Chapman, D. C. (2003), Separation of an advectively trapped buoyancy current at a bathymetric bend, *J. Phys. Oceanogr.*, *33*, 1108–1121.
- Chapman, D. C., and R. C. Beardsley (1989), On the origin of shelf water in the Middle Atlantic Bight, *J. Phys. Oceanogr.*, *19*, 384–391.
- Chapman, D. C., and S. J. Lentz (1994), Trapping of a coastal density front by the bottom boundary layer, *J. Phys. Oceanogr.*, *24*, 1464–1479.
- Chen, C. (1992), Variability of currents in Great South Channel and over Georges Bank, *Tech. Rep. WHOI-92-20*, 283 pp., MIT/WHOI Joint Program, Woods Hole, Mass.
- Chen, C. (2000), A modeling study of episodic cross-frontal water transports over the inner shelf of the South Atlantic Bight, *J. Phys. Oceanogr.*, *30*, 1722–1742.
- Chen, C., and R. C. Beardsley (1995), A numerical study of stratified tidal rectification over finite amplitude banks. part I: Symmetric banks, *J. Phys. Oceanogr.*, *25*, 2090–2110.
- Chen, C., and R. C. Beardsley (1998), Tidal mixing and across-frontal particle exchange over a finite amplitude asymmetric bank: A model study with application to Georges Bank, *J. Mar. Res.*, *56*, 1163–1201.
- Chen, C., R. C. Beardsley, and D. Limeburner (1995), A numerical study of stratified tidal rectification over finite amplitude banks. part II: Georges Bank, *J. Phys. Oceanogr.*, *25*, 2111–2128.
- Chen, C., L. Zheng, and J. O. Blanton (1999), Physical processes controlling the formation, evolution, and perturbation of the low-salinity front in the inner shelf off the southeastern United States: A modeling study, *J. Geophys. Res.*, *104*, 1259–1288.
- Chen, C., J. Zhu, E. Ralph, S. A. Green, and J. Budd (2001a), Prognostic modeling studies of the Keweenaw current in Lake Superior. part I: Formation and evolution, *J. Phys. Oceanogr.*, *31*, 379–395.
- Chen, C., R. C. Beardsley, and P. J. S. Franks (2001b), A 3-D prognostic model study of the ecosystem over Georges Bank and adjacent coastal regions. part I: Physical model, *Deep Sea Res., Part I*, *48*, 419–456.
- Chen, C., H. Liu, and R. C. Beardsley (2003a), An unstructured, finite volume, three-dimensional, primitive equation ocean model: Application to coastal ocean and estuaries, *J. Atmos. Oceanic Technol.*, *20*, 159–186.
- Chen, C., R. C. Beardsley, P. J. S. Franks, and J. Van Keuren (2003b), Influence of diurnal heating on stratification and residual circulation of Georges Bank, *J. Geophys. Res.*, *108*(C11), 8008, doi:10.1029/2001JC001245.
- Chen, C., J. Zhu, L. Zheng, E. Ralph, and J. W. Budd (2004a), A non-orthogonal primitive equation coastal ocean circulation model: Application to Lake Superior, *J. Great Lake Res.*, *30*, 41–54.
- Chen, C., G. Cowles, and R. C. Beardsley (2004b), An unstructured grid, finite volume coastal ocean model: FVCOM User Manual, *Tech. Rep. 04-0601*, 183 pp., School for Mar. Sci. and Technol. (SMAST)/Univ. of Mass.-Dartmouth (UMASSD), New Bedford, Mass.
- Cockburn, B., S. Hou, and C. W. Shu (1990), TVB Runge-Kutta local projection discontinuous Galerkin finite element method for conservation laws IV: The multidimensional case, *Math. Comput.*, *54*, 545–581.
- Csanady, G. T. (1968), Motions in a model great lake due to suddenly imposed wind, *J. Geophys. Res.*, *73*, 6435–6447.
- Dupont, D., C. G. Hannah, and D. Greenberg (2005), Modeling the sea level of the upper Bay of Fundy, *Atmos. Ocean*, *43*, 33–47.
- Dupont, F., D. N. Straub, and C. A. Lin (2003), Influence of a step-like coastline on the basin scale vorticity budget of mid-latitude gyre models, *Tellus, Ser. A*, *55*, 255–272.
- Egbert, G. D., and S. Y. Erofeeva (2002), Efficient inverse modeling of barotropic ocean tides, *J. Atmos. Oceanic Technol.*, *19*(2), 183–204.
- Galperin, B., L. H. Kantha, S. Hassid, and A. Rosati (1988), A quasi-equilibrium turbulent energy model for geophysical flows, *J. Atmos. Sci.*, *45*, 55–62.
- Garrett, C. J. (1972), Tidal resonance in the Bay of Fundy and Gulf of Maine, *Nature*, *238*, 441–443.
- Garvine, R. W. (1999), Penetration of buoyant coastal discharge onto the continental shelf, *J. Phys. Oceanogr.*, *29*, 1892–1909.
- Greenberg, D. A. (1979), A numerical model investigation of tidal phenomena in the Bay of Fundy and Gulf of Maine, *Mar. Geod.*, *2*, 161–187.
- Greenberg, D. (1983), Modelling the mean barotropic circulation in the Bay of Fundy and Gulf of Maine, *J. Phys. Oceanogr.*, *13*, 886–904.
- Haidvogel, D. B. and A. Beckmann (1999), *Numerical Ocean Circulation Modeling*, 318 pp., Imperial College Press, London.
- Haidvogel, D. B., H. G. Arango, K. Hedstrom, A. Beckmann, P. M. Rizzoli, and A. F. Schepetkin (2000), Model evaluation experiments in the North Atlantic Basin: Simulation in nonlinear terrain-following coordinates, *Dyn. Atmos. Oceans*, *32*, 239–281.
- Haney, R. L. (1991), On the pressure gradient force over steep topography in sigma coordinate ocean models, *J. Phys. Oceanogr.*, *21*, 610–619.
- Hubbard, M. E. (1999), Multidimensional slope limiters for MUSCL-type finite volume schemes on unstructured grids, *J. Comput. Phys.*, *155*, 54–74.
- Hughes, T., G. Engel, L. Mazzei, and M. Larson (2000), A comparison of discontinuous and continuous Galerkin methods, in *First International Symposium on Discontinuous Galerkin Methods, Lecture Notes in Computational Science and Engineering*, vol. 11, edited by B. Cockburn, G. E. Karniadakis, and C. W. Shu, pp. 135–146, Springer, New York.
- Kobayashi, M. H., J. M. C. Pereira, and J. C. F. Pereira (1999), A conservative finite volume second-order-accurate projection method on hybrid unstructured grids, *J. Comput. Phys.*, *150*, 40–45.
- Kourafalou, V. H., L.-Y. Oey, J. D. Wang, and T. N. Lee (1996), The fate of river discharge on the continental shelf: 1. Modeling the river plume and the inner shelf coastal current, *J. Geophys. Res.*, *101*, 3415–3434.
- Kraus, E. B. (1972), *Atmosphere-Ocean Interaction*, 275 pp., Clarendon, Oxford, U. K.
- Limeburner, R., and R. C. Beardsley (1996), Near-surface recirculation on Georges Bank, *Deep Sea Res., Part II*, *43*, 1547–1574.
- Loder, J. (1980), Topographic rectification of tidal currents on the sides of Georges Bank, *J. Phys. Oceanogr.*, *10*, 1399–1416.
- Lynch, D. R., and C. E. Naimie (1993), The M<sub>2</sub> tide and its residual on the outer banks of the Gulf of Maine, *J. Phys. Oceanogr.*, *23*, 2222–2253.
- Maday, Y. and A. T. Patera (1988), Spectral element methods for the incompressible Navier-Stokes equations, in *State-of-the-Art Surveys in Computational Mechanics*, edited by A. K. Noor, pp. 71–143, ASME, New York.
- Mellor, G. L., and T. Yamada (1982), Development of a turbulence closure model for geophysical fluid problem, *Rev. Geophys.*, *20*, 851–875.
- Mellor, G. L., T. Ezer, and L.-Y. Oey (1994), The pressure gradient conundrum of sigma coordinate ocean models, *J. Ocean. Atmos. Technol.*, *11*, 1126–1134.
- Mesinger, F. and A. Arakawa (1976), *Numerical Methods Used in Atmospheric Models, GARP Publ. Ser.*, vol. 1, WMO-ICSU Joint Organizing Comm., Univ. of Calif., Los Angeles.
- Naimie, C. E. (1996), Georges Bank residual circulation during weak and strong stratification periods: Prognostic numerical model results, *J. Geophys. Res.*, *101*, 6469–6486.
- Naimie, C. E., J. W. Loder, and D. R. Lynch (1994), Seasonal variation of the three-dimensional residual circulation on Georges Bank, *J. Geophys. Res.*, *99*, 15,967–15,989.
- Pedlosky, J. (1974), Longshore currents, upwelling and bottom topography, *J. Phys. Oceanogr.*, *4*, 214–226.
- Phillips, O. M. (1970), On flows induced by diffusion on a stably stratified fluid, *Deep Sea Res. Oceanogr. Abstr.*, *17*, 435–443.
- Reed, W. H. and T. R. Hill (1973), Triangular and methods for the neutron transport equation, *Tech. Rep. LA-UR-73-479*, Los Alamos Sci. Lab., Los Alamos, N. M.
- Simpson, J. J., and T. D. Dickey (1981a), The relationship between downward irradiance and upper ocean structure, *J. Phys. Oceanogr.*, *11*, 309–323.
- Simpson, J. J., and T. D. Dickey (1981b), Alternative parameterizations of downward irradiance and their dynamical significance, *J. Phys. Oceanogr.*, *11*, 876–882.
- Smagorinsky, J. (1963), General circulation experiments with the primitive equations, I. The basic experiment, *Mon. Weather Rev.*, *91*, 99–164.

- Smolarkiewicz, P. K. (1984), A fully multidimensional positive definite advection transport algorithm with small implicit diffusion, *J. Comput. Phys.*, *54*, 325–362.
- Smolarkiewicz, P. K., and T. L. Clark (1986), The multidimensional positive definite advection transport algorithm: Further development and applications, *J. Comput. Phys.*, *86*, 355–375.
- Song, Y. T., and D. G. Wright (1998), A general pressure gradient formulation for ocean models. part II: Energy, momentum and bottom torque consistency, *Mon. Weather Rev.*, *126*, 3131–3247.
- Wunsch, C. (1970), On oceanic boundary mixing, *Deep Sea Res. Oceanogr. Abstr.*, *17*, 293–301.
- Zhu, J., C. Chen, E. Ralph, and S. A. Green (2001), Prognostic modeling studies of the Keweenaw current in Lake Superior. part II: Simulation, *J. Phys. Oceanogr.*, *31*, 396–410.
- 
- R. C. Beardsley, Department of Physical Oceanography, Woods Hole Oceanographic Institution, Woods Hole, MA 02543, USA.
- C. Chen, G. Cowles, H. Huang, H. Liu, and Q. Xu, School of Marine Sciences and Technology (SMAST), University of Massachusetts-Dartmouth, 706 South Rodney French Boulevard, New Bedford, MA 02744-1221, USA. (c1chen@umassd.edu)